Structural Characterization of Oleylamine and Dodecanethiol Capped Ge_{1-x}Sn_x Alloy Nanocrystals

Kathryn A. Newton,† Heather Renee Sully,‡ Frank Bridges,§ Sue A. Carter,§ and Susan M. Kauzlarich*,†

- † Department of Chemistry, One Shields Avenue, University of California, Davis, CA 95616
- [‡] Department of Electrical Engineering, University of California, Santa Cruz, California 95064
- § Department of Physics, University of California, Santa Cruz, California 95064
- *smkauzlarich@ucdavis.edu

ABSTRACT: Microwave-assisted heating methods have been used to synthesize oleylamine-capped $Ge_{1-x}Sn_x$ nanocrystals. By varying the reaction temperature while keeping the Ge and Sn precursor concentrations constant, $Ge_{1-x}Sn_x$ nanocrystals with Sn compositions of 13.9 ± 2.1 % over the 3.8 to 9.3 nm size range have been achieved. The oleylamine capping ligand is replaced with dodecanethiol without affecting the Sn composition of the nanocrystals. The Sn composition is obtained from employing Vegard's law on the lattice parameters obtained from the Rietveld refinement of powder X-ray diffraction patterns. STEM provides particle size and morphology. Extended X-ray absorption fine structure (EXAFS) at the Sn and Sn and Sn and Sn and Sn are used to characterize the surface ligand capping before and after ligand exchange. Tauc plot analysis of Sn nanocrystals is reported. This work demonstrates the effects of synthesis temperature on the particle size, composition, and structure of Sn ananocrystals.

INTRODUCTION

Band gap engineering of Ge nanocrystals (NCs) can be achieved through alloying. It has been predicted that incorporation of Sn in a cubic Ge_{1-x}Sn_x alloy structure would result in an indirect-to-direct band gap crossover.1-9 Incorporation of the zero-gap semiconductor Sn lowers the overall energy of the conduction band of Ge, and the energy of the Γ point (k = 0) is predicted to decrease more rapidly than that of the L point $(k \neq 0)$, making the direct band gap transition lower in energy for the alloy.5 Using Vegard's law and assuming properties are linearly dependent on composition, indirect-to-direct crossover has been interpolated to occur at x = 0.22 for $Ge_{1-x}Sn_x$. 10, 11 Other theoretical predictions place the indirect-to-direct crossover for unstrained $Ge_{1-x}Sn_x$ at Sn compositions ranging from x = 0.016 to $0.17,^2$ $^{3, 6, 9, 10, 12-15}$ with the range of x = 0.06 to 0.11 being generally accepted.16-20 Computational studies have been employed to better understand the band structure and emission properties of Ge_{1-x}Sn_x NCs.^{8, 16, 18, 19} Emission similar in energy to the absorption onset is attributed to a fundamental energy gap transition, and non-radiative decay can occur from surface trap states caused by Sn incorporation and alloy disorder. 16,

Microwave-assisted heating has been applied to the synthesis of doped and alloyed Ge nanomaterials. Bismuth-

doped Ge NCs were synthesized by microwave-assisted reduction of GeI_2 and $BiCI_3$. 21 , 22 Similar to the incorporation of Bi in Ge structures, the synthesis of $Ge_{1-x}Sn_x$ nanomaterials is challenging due to the low solubility of Sn in Ge (< 1% Sn) and a large lattice mismatch that makes the alloy thermodynamically unstable. $^{21-26}$ $Ge_{1-x}Sn_x$ nanowires have been synthesized by the microwave-assisted reduction of bis[bis(trimethylsilyl)amino]tin(II) and bis[bis(trimethylsilyl)amino]germanium(II). 20 , 27 $Ge_{1-x}Sn_x$ NCs have also been achieved by the microwave-assisted reduction of GeI_2 and bis[bis(trimethylsilyl)amino]tin(II) in oleylamine (OAm); however, synthesis using convection heating has been studied more extensively. $^{16-20}$, 24 , 25 , $^{27-31}$

Ge-rich $Ge_{1-x}Sn_x$ NCs with diameters of 2.5 to 21 nm and Sn compositions of $0.015 \le x \le 0.42$ have been achieved with the reduction of Gel_2 and $SnCl_2$ or bis[bis(trimethylsily])amino]tin(II) in OAm or hexadecylamine, with the higher Sn compositions achieved with the addition of a reducing agent. $Sncondotate{16}$, $Sncondotate{17}$, $Sncondotate{28}$, $Sncondotate{29}$ For synthesis by convection heating, $Sncondotate{17}$ NC size and composition have been shown to depend on reaction temperature, time, and the concentration of the tin(II) precursor. $Sncondotate{29}$ For reactions below $Sncondotate{20}$ For higher temperature reactions, size increases but $Sncondotate{29}$ For higher temperature reactions, size increases but $Sncondotate{29}$ For higher temperature reactions, size increases but $Sncondotate{29}$ for higher temperature reactions, size increases but $Sncondotate{20}$ for higher temperature reactions, size increases but $Sncondotate{20}$ for higher temperature reactions, size increases but $Sncondotate{20}$ for higher temperature reactions, size increases $Sncondotate{20}$ for higher temperature reactions and decreased $Sncondotate{20}$ f

 $Ge_{1-x}Sn_x$ NCs with Sn compositions of $0 \le x \le 0.95$ have been achieved using a hot injection method.³⁰ A mechanistic study of this reaction suggests the NC formation begins with the reduction of Sn clusters into Sn nanodroplets with Sn-Ge complexes at the surface. Ge atoms are proposed to diffuse into the nanodroplets, forming areas of proeutectic phase that stabilize the core of the nanoparticle while growth proceeds by decomposition of the Sn-Ge metal complexes on the particle surface. More recently, narrow size distributions have been achieved by the addition of hexadecylamine to control particle growth or by templating with Sn nanoparticles.^{24, 25} The composition of Ge_{1-x}Sn_x NCs synthesized by the injection of a solution of GeI2 in trioctylphosphine into a solution of Sn nanoparticles was observed to be dependent on reaction time.²⁵ Despite these synthetic advances, indirect-to-direct crossover has not been observed in Ge1-xSnx NCs, and band gap tunability remains a challenge.

Although the microwave-assisted synthesis of Ge_{1-x}Sn_x NCs has been reported in the literature, additional studies in which temperature, time, and precursor concentration are systematically varied are necessary to fully understand the effects of microwave-assisted synthesis conditions on NC size, composition, structure, and surface functionalization. This work presents a detailed study of the effects of temperature in the microwave-assisted synthesis of Ge1-_xSn_x NCs. For Ge_{1-x}Sn_x NCs direct ligand exchange methods have been demonstrated to result in a partial replacement of the OAm ligand for films and solutions of NCs.28 and it has been shown that Ge_{1-x}Sn_x NCs can be protected with a CdS shell or a thin coating of GeS.33 In this work, a hydrazineassisted ligand exchange method, previoulsy applied to Ge and Bi-doped Ge NCs, is used to achieve thiol passivation of Ge_{1-x}Sn_x NCs synthesized at a range of temperatures. ^{21, 22, 32}-35 Following ligand exchange, the local structure of GeSn NCs was characterized by extended X-ray absorption fine structure (EXAFS). EXAFS can probe the local environment about alloy or dopant atoms in the structure of metastable nanomaterials. EXAFS has demonstrated that Bi occupies surface substitutional sites in Bi-doped Ge NCs and that disorder increases with Bi composition. ²² It was also observed that order could be partially restored through ligand exchange Here, EXAFS is applied to Ge_{1-x}Sn_x NCs to gain understanding of their physical and structural properties that is fundamental to advancing band gap engineering of these materials.7

To study the effects of reaction temperature on particle size, composition, and structure, $Ge_{1-x}Sn_x$ NCs were prepared by microwave-assisted reduction of GeI_2 and bis[bis(trimethylsilyl)amino]tin(II) in OAm at temperatures from 210 to 280 °C. A hydrazine-assisted ligand exchange was used to passivate the NC surface with dodecanethiol (DDT). Both composition and size are conserved through ligand exchange. NC composition and structure are characterized by powder X-ray diffraction (PXRD), scanning transmission electron microscopy (STEM), and Raman spectroscopy. Local atomic structure and composition of the DDT capped $Ge_{1-x}Sn_x$ NCs are characterized by EXAFS. Surface ligand passivation is characterized by Fourier-transform infrared spectroscopy (FTIR) and proton nuclear magnetic resonance spectroscopy (¹H NMR). The effects of

ligand exchange and surface passivation on band gap energy are demonstrated with UV-Vis-NIR spectroscopy.

METHODS

Chemicals

Germanium(II) iodide (GeI₂) was purchased from Professor Richard Blair's laboratory at the University of Central Florida.³⁶ Oleylamine $(CH_3(CH_2)_7CHCH(CH_2)_8NH_2, \ge 98\%$, Sigma-Aldrich) and dodecanethiol (CH₃(CH₂)₁₀CH₂SH, ≥ 98%, Sigma-Aldrich) were dried over 3 Å molecular sieves for several days and degassed by heating at 150 °C under vacuum for 2 h before use. Bis[bis(trimethylsilyl)amino]tin(II) ([[(CH₃)₃Si]₂N]₂Sn, 95%, Gelest), hydrazine (N₂H₄, anhydrous, 98%, Sigma-Aldrich), ethanol (CH₃CH₂OH, anhydrous, ≥ 99.5%, Sigma-Aldrich), methanol (CH₃OH, anhydrous, ≥ 99.5%, Sigma-Aldrich), and deuterated chloroform (CDCl₃, 99.8 atom% D, Cambridge Isotope Laboratories) were used as received. Toluene, hexane, and acetonitrile (HPLC grade, Sigma Aldrich) were passed through a solvent still prior to use. All chemicals, except deuterated chloroform, were stored in an argon-filled glovebox. Hydrazine should be handled in an inert environment; it is acutely toxic, carcinogenic, and has a very low flashpoint (52 °C).

Microwave-Assisted Synthesis

In an argon-filled glovebox 20 mL of oleylamine (OAm) was added to 2.0 mmol of GeI2 in a 35 mL CEM microwave tube with a stir bar and sealed with a Teflon cap. The mixture was sonicated outside the glovebox to form a transparent yellow solution and was returned to the glovebox, where 2.0 mmol of bis[bis(trimethylsilyl)amino]tin(II) dissolved in 10 mL of OAm was added. This 30 mL solution of GeI2 and bis[bis(trimethylsilyl)amino]tin(II) in OAm was divided into 6 mL aliquots. Each aliquot was placed in a 35 mL microwave tube with a stir bar, capped, and transferred to a microwave reactor. The solutions were heated at temperatures of 210, 220, 230, 240, and 250 °C for 30 min in dynamic heating mode using a CEM Discover microwave (CEM Corporation) equipped with a CEM Explorer autosampler. A similar procedure was used for syntheses at 260, 270, and 280 °C. All reactions produced dark brown suspensions of Ge_{1-x}Sn_x NCs passivated with OAm ligands. In the glovebox, each suspension was transferred to a centrifuge tube using 4 mL of hexane, and varying amounts of anhydrous ethanol and anhydrous methanol were added as antisolvents. Each mixture was centrifuged at 8500 RPM for 10 minutes, yielding a colorless solution and dark precipitate. The supernatant was decanted in the glovebox. The precipitate was dispersed in hexane or toluene, and varying amounts of antisolvent were added as needed to achieve a dark precipitate and nearly colorless supernatant following centrifugation. Additional precipitations, in which antisolvents were added to the dispersed NCs before centrifugation for 10 min at 8500 RPM, were performed as necessary to obtain powder X-ray diffraction patterns free of β-Sn impurities. Most samples were precipitated a total of two to three times, or until no extra peaks, aside from the diamond cubic Ge1-xSnx peaks, were apparent in the PXRD. After precipitation, the supernatant was decanted, and the dark brown Ge_{1-x}Sn_x NC precipitate was redispersed in 7 mL of hexane and stored in an argon-filled glovebox.

Ligand Exchange

A ligand exchange procedure was performed on 3 mL aliquots of each Ge_{1-x}Sn_x NC solution to replace OAm with dodecanethiol (DDT). In an argon-filled glovebox, an equal volume of 5 M hydrazine in acetonitrile was added to 3 mL of Ge_{1-x}Sn_x NC solution. The mixture was sonicated for 90 min outside the glovebox. In the glovebox, 4 mL of toluene was added to homogenize the solution before centrifugation at 8500 RPM for 10 min. The dark brown precipitate was collected, and the clear, colorless liquid phase was decanted. To remove residual hydrazine, the Ge_{1-x}Sn_x NC precipitate was briefly sonicated with 5 mL of acetonitrile and centrifuged at 8500 RPM for 5 min. After decanting the supernatant, the precipitate was resuspended in 5 mL of hexane and separated without centrifugation to remove any particles with residual OAm-capping. Using this procedure, the precipitate was washed with hexane a total of 3 times. In the glovebox, 6 mL of DDT was added to the Ge_{1-x}Sn_x NC precipitate, and the solution was heated at 150 °C for 60 min in dynamic heating mode using a CEM Discover microwave equipped with a CEM Explorer autosampler. The resulting solution was washed in the glovebox with 4 mL of hexane and varying amounts of anhydrous ethanol and anhydrous methanol as antisolvents. Following centrifugation at 8500 RPM for 10 min, the clear, nearly colorless supernatant was decanted, and the brown Ge1-xSnx NC precipitate was dispersed in 3.5 mL of hexane. All DDT-capped Ge_{1-x}Sn_x NC products were stored in an argon-filled glovebox.

Powder X-ray Diffraction (PXRD)

Powder X-ray diffraction patterns were collected on a Bruker D8 Advance diffractometer (Bruker Corporation) using Cu Kα radiation (40 kV, 40 mA). The NC dispersions were deposited on a silica zero-background holder and dried before data collection. Patterns were collected both with and without a small amount of NIST silicon standard reference material (SRM) 640B, which was employed as a reference for Rietveld refinement. Data were collected in air in the 2θ range of $10-80^{\circ}$ with a step size of 0.02° . The crystallite diameter was determined from the (220) reflection using a Scherrer analysis in MDI Jade 5.0 software.³⁷ Patterns were compared to reference powder diffraction files (PDFs) from the International Center for Diffraction Data (ICDD). Rietveld refinement in Jana2006 software was used to obtain lattice parameters from powder patterns collected with Si SRM 640B.38, 39 Crystallographic information files used in Rietveld refinement were obtained from the Inorganic Crystal Structure Database (ICSD).40

Scanning Transmission Electron Microscopy (STEM) and Energy Dispersive X-ray Spectroscopy (EDS)

Ultrathin carbon film on lacey carbon support film on 400 mesh copper grids (Ted Pella Inc.) were used for STEM imaging. Dispersions of NCs in hexane were drop-cast on the grids and dried overnight in a 120 °C vacuum oven. STEM imaging was performed on an aberration-corrected JEOL JEM-2100AC transmission electron microscope (JEOL Ltd.) equipped with a Gatan annular dark field (ADF) detector (Gatan Inc.). Particles were imaged in high angle annular dark field (HAADF) and bright field STEM imaging modes with camera lengths of 10 or 12 cm. STEM images were collected using Digital Micrograph software. Image J software was used to measure the minimum and maximum Feret

diameters of approximately 500 unique NCs on each specimen grid.⁴¹ Particle diameters are reported as the geometric mean of the minimum and maximum Feret diameters. EDS was performed in STEM mode using an Oxford X-MaxN TSR EDS detector (Oxford Instruments) attached to the JEOL JEM-2100AC. EDS line scans, maps, and spectra were collected with Aztec imaging software.⁴²

Extended X-ray Absorption Fine Structure (EXAFS)

Ge_{1-x}Sn_x NCs for extended X-ray absorption fine structure (EXAFS) measurements were synthesized at 230, 240, or 250 °C and re-passivated with DDT by the synthesis and ligand exchange procedures previously described. The samples for EXAFS were also characterized by PXRD, FTIR, and UV-Vis-NIR spectroscopy. Specimens for EXAFS studies were prepared in an argon-filled glovebox by pipetting the Ge_{1-x}Sn_x NCs, dispersed in hexane, onto a 3 × 12 mm² piece of filter paper and then evaporating the solvent at room temperature. The process of pipetting and evaporating was repeated to deposit 5.9 mg of NCs with even coverage. After drying, each specimen was sealed between pieces of 3M ® 600 Transparent Scotch Tape, which is transparent to X-rays, to prevent oxidation during transport and data collection

EXAFS measurements were performed at the Stanford Synchrotron Radiation Lightsource (SSRL) on beam line 4-1, using a Si (220) double crystal monochromator (phi = 0) and detuning 30% for all edges. The ring was operating at 500 mA current. All fluorescence data were collected using a 30 channel Ge detector, and reference data for Ge bulk powder and Sn foil standards were collected simultaneously. At the Ge K edge (E = 11,103 eV), data were collected in transmission mode with $0.5 \times 6.0 \text{ mm}^2$ slits to give a 1.1 eV energy resolution. Data were collected in transmission and fluorescence modes at the Sn K edge (E = 29,200 eV) with $0.2 \times 4.0 \text{ mm}^2$ slits, giving an energy resolution of 3.2eV. For fluorescence measurements, specimens were placed at a 45° angle to the X-ray beam. Specimens were held in an Oxford helium cryostat with the temperature maintained at 10 K to minimize thermal disorder. Spectra were collected up to wavenumber, $k = 15 \text{ Å}^{-1}$ for Ge and 14 Å⁻¹ for Sn, and 3-4 scans were collected and averaged for each specimen.

EXAFS data were reduced using standard procedures in the R-Space X-ray Absorption Package (RSXAP).43 First, glitches were removed, and then the pre-edge background was subtracted. The step-height was then normalized, and the post-edge was subtracted to extract the EXAFS oscillations. The data were transformed into k-space and then into real space (r-space) by a fast Fourier transform (FFT) using an FT range of 3.5-14.5 Å-1 for Ge and 3.5-13.5 Å-1 for Sn. In r-space, the spectra were fit to a sum of theoretical functions calculated using the code FEFF7.44 For the Ge K edge, Sn atoms were substituted on undistorted first and second nearest neighbor lattice sites, and theoretical standards, $k*\chi(k)$, for Ge-Ge and Ge-Sn atom pairs were generated. For the Sn K edge, Sn atoms were placed at the origin and on the first and second nearest neighbor lattice sites, and the theoretical standards for Sn-Ge and Sn-Sn atom pairs were calculated. Bond length expansions were allowed to account for the larger atomic radius of Sn relative to Ge.

Raman Spectroscopy

Raman spectra were collected using a Renishaw RM1000 laser Raman microscope (Renishaw PLC) with a 514 nm excitation wavelength. The instrument is equipped with a motorized stage. Dispersions of NCs were deposited on aluminum foil and air-dried prior to data collection. Experimental data were analyzed using Mathematica 11.0.1.0 software and a Raman analysis notebook written for use in Mathematica. Experimental spectra were fit as the sum of two Lorentzian functions and a linear baseline function to obtain the peak shift and the full width at half maximum. 46

Proton Nuclear Magnetic Resonance Spectroscopy (1H NMR)

To prepare samples for $^1\mathrm{H}$ NMR, 0.5 mL of NC dispersion was heated to dryness in a vacuum oven at 100 °C for 3 h. In an argon-filled glovebox the dry NCs were redispersed in 0.5 mL of d-chloroform and transferred to an NMR tube. $^1\mathrm{H}$ NMR spectra were collected at room temperature using a 400 MHz Bruker Nanobay AVIIIHD. Spectral analysis was performed using MestReNova Version: 10.0.2-15465 software. 47

Fourier-transform Infrared (FTIR) and UV-Vis-NIR Spectroscopy

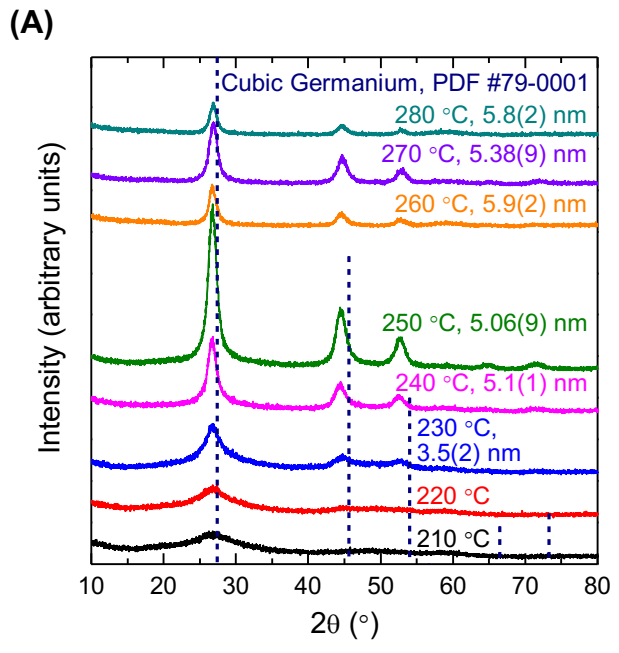
FTIR spectra were collected on a Bruker Alpha-P (Bruker Corporation) from 4500 to 375 cm⁻¹. NC dispersions were deposited on the instrument's attenuated total reflectance (ATR) chip and allowed to dry before data collection.

Transmittance UV-Vis-NIR spectra were collected for NCs in dilute hexane dispersions using a Shimadzu UV-3600 UV-Vis-NIR spectrophotometer (Shimadzu Corporation). Spectra were collected in dual-beam mode from 1600 to 290 nm in quartz cuvettes, and the solvent background was subtracted. Band gap analysis was performed using Mathematica 11.0.1.0 and a UV-Vis-NIR analysis notebook written for use in Mathematica.⁴⁵ Transmittance data were collected as a function of the incident wavelength in nanometers and replotted versus energy of the incident wavelength in electronvolts. Transmittance data were converted to absorbance, and Tauc plots were generated using the relationship $E(eV) = (hv * A)^{\frac{1}{n}}$, where n = 2 for allowed indirect transitions and $n = \frac{1}{2}$ for allowed direct transitions.⁴⁸ Each data set was fit with a seventh order polynomial function, and the first and second derivatives were calculated. A seventh order polynomial has five inflection points, giving five possible tangent lines. The lowest energy inflection point is unreliable due to low absorbance at low energy and scattering. The highest energy inflection point is erroneous. The equation of the tangent line was determined for the remaining three inflections points. The indirect band gap was determined as the x-intercept of the tangent line with the greatest slope.

RESULTS & DISCUSSION

Characterization of Structure and Composition

 $_xSn_x$ NCs prepared at the various temperatures, along with the corresponding DDT-capped $Ge_{1-x}Sn_x$ NCs, are shown in Figure 1. The patterns show that the indicated cubic Ge peaks are shifted from the expected positions to lower



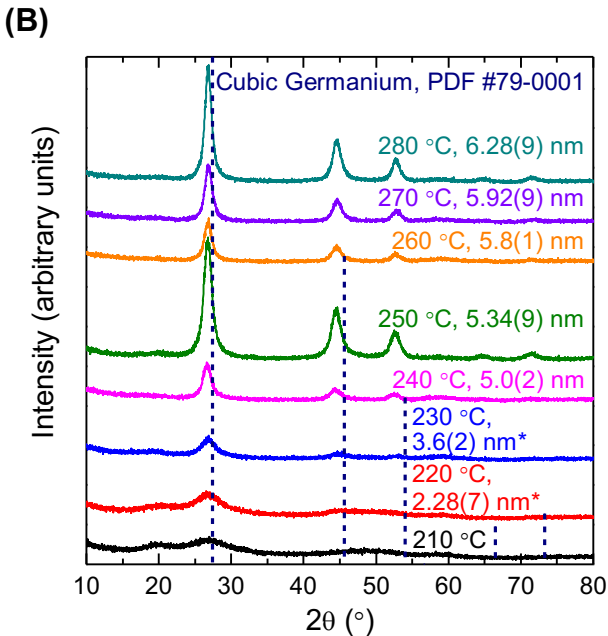


Figure 1. PXRD patterns of (A) OAm- (B) DDT-capped $Ge_{1-x}Sn_x$ NCs synthesized with equal molar amounts of Gel_2 and bis[bis(trimethylsilyl)amino]tin(II) at the indicated temperatures. Patterns are compared to the reference pattern of cubic Ge (ICDD PDF #79-0001, dark-blue dashed lines). Crystallite diameter is given in nm and is obtained from the Scherrer equation based on the (220) reflection (27.4°) or the (111) reflection (45.6°) when indicated with an asterisk.

angles due to the incorporation of Sn in the structure, consistent with a cubic $Ge_{1-x}Sn_x$ alloy structure. There is no evidence for α - or β -Sn impurities for the samples prepared at

the various temperatures. PXRD patterns were also collected of OAm-capped $Ge_{1-x}Sn_x$ NCs that were precipitated only one time (Figure S1 in the Supporting Information). In

addition to diffraction peaks consistent with the cubic Ge1- $_x Sn_x$ alloy structure, peaks consistent with $\beta\text{-Sn}$ are

Table 1. Crystallite Diameter, Lattice Parameter (a), Sn Composition, and Particle Diameter for OAm- and DDT-capped $Ge_{1-x}Sn_x$ NCs Synthesized at 210-280 °C^a

Synthesis Temperature (°C)		Crystallite Diameter (nm)	а (Å)	Sn Composition (% Sn)	Particle Diameter (nm)	
	210		5.738(8)	11.8 ± 1.1	3.8 ± 1.1	
	220		5.741(6)	12.3 ± 0.8	4.0 ± 1.1	
OAm	230	3.5 ± 0.2	5.753(2)	14.0 ± 0.3	4.4 ± 1.3	
	240	5.1± 0.1	5.7817(8)	17.9 ± 0.1	5.5 ± 2.6	
	250	5.06 ± 0.09	5.7630(5)	15.36 ± 0.08	7.5 ± 2.6	
	260	5.9 ± 0.2	5.760(1)	15.0 ± 0.2	9.3 ± 3.1	
	270	5.38 ± 0.09	5.7383(7)	11.9 ± 0.1	8.2 ± 1.7	
	280	5.8 ± 0.2	5.748(2)	13.2 ± 0.2	9.0 ± 2.2	
	210		5.701(9)	6.5 ± 1.3	3.4 ± 0.7	
	220	2.28 ± 0.07*	5.742(5)	12.5 ± 0.7	3.8 ± 1.2	
	230	3.6 ± 0.2*	5.754(3)	14.1 ± 0.4	4.7 ± 1.6	
T	240	5.0 ± 0.2	5.786(1)	18.5 ± 0.2	6.8 ± 2.1	
Taa	250	5.34 ± 0.09	5.7580(5)	14.65 ± 0.08	8.1 ± 2.5	
	260	5.8 ± 0.1	5.7587(9)	14.8 ± 0.1	8.3 ± 2.5	
	270	5.92 ± 0.09	5.7496(6)	13.47 ± 0.08	9.5 ± 2.5	
	280	6.28 ± 0.09	5.7551(4)	14.24 ± 0.07	8.7 ± 3.0	

^a The crystallite diameter was determined by Scherrer analysis of the (220) reflection or the (111) reflection when indicated by an asterisk. The corresponding Sn composition (% Sn) was calculated from lattice parameter a (Å), which was refined from PXRD patterns. Particle diameter was determined by analysis of STEM images.

observed. Additional precipitations remove these impurities. Peak narrowing is observed in the powder diffraction patterns as the reaction temperature is increased, suggesting that size and crystallinity are increasing. Crystallite diameter is calculated by Scherrer analysis of the (220) X-ray diffraction peak and is observed to increase with reaction temperature (Table 1). Ligand exchange does not result in phase segregation, and there is little change in crystallite diameter. Crystallite diameter of the DDT-capped Ge_{1-x}Sn_x NCs synthesized at 230, 240, 260, and 280 °C are within three standard deviations of the corresponding OAm-capped crystallite diameters.

OAm- and DDT-capped $Ge_{1-x}Sn_x$ NCs displayed lattice parameters between those of cubic Ge (5.65675(1) Å) and α -Sn (6.4892(1) Å) (Figures S2-S3 and Table S1 in the Supporting Information).^{49,50} Lattice parameters were used to calculate the Sn composition (% Sn) of each sample according to Vegard's law, given in Equation 1, with bowing parameter b=0.166, as established by Aella et al. and previously used for the characterization of $Ge_{1-x}Sn_x$ NCs by Ramaswamy et al.^{11,29,51}

Equation 1.
$$a_{Ge_{1-x}Sn_x} = a_{Ge}(1-x) + a_{Sn}x - bx(1-x)$$

The results are summarized in Table 1 and are consistent with the values for $Ge_{1-x}Sn_x$ NCs reported in the

literature. ^{17, 29} Figure 2 shows a plot of the lattice parameters and the corresponding Sn compositions as a function of reaction temperature. The Sn composition increases with

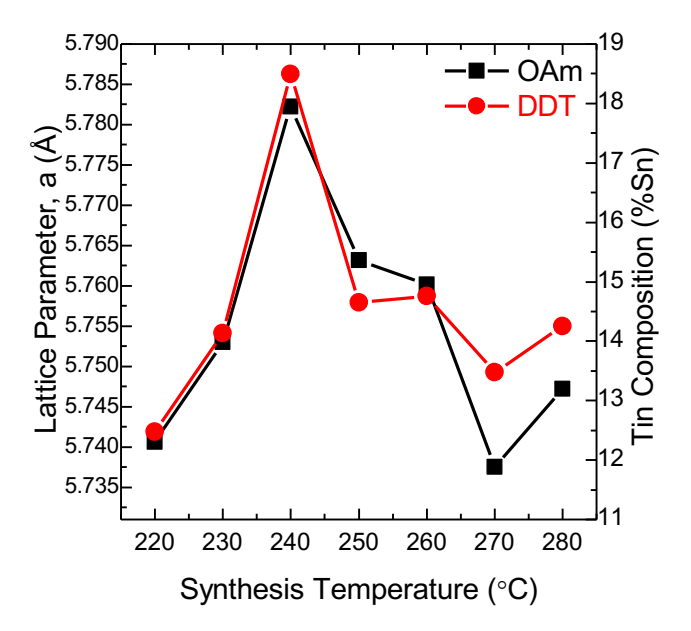


Figure 2. Lattice parameters and corresponding Sn composition from Vegard's law as a function of synthesis temperature for OAm- and DDT-capped Ge_{1-x}Sn_x NCs.

temperature until 240 °C and then decreases, providing Sn compositions from 11.8% to 17.9%. Sn composition likely decreases at higher temperatures due to surpassing the melting point of Sn. Following ligand exchange, only small changes in lattice parameter and, therefore, Sn composition are observed.

STEM-EDS was used to confirm the elemental composition of the DDT-capped Ge_{1-x}Sn_x NCs synthesized at 250 and 270 °C with equal molar amounts of GeI2 and bis[bis(trimethylsilyl)amino]tin(II). The particle diameter for these samples is given in Table 1. A representative EDS linescan is shown in Figure 3 for the 250 °C reaction and in Figure S4 (in the Supporting Information) for the 270 °C reaction. From the line scan spectra, composition was determined to be 15.3 ± 1.1 atom% Sn for both reactions (Figure S4 in the Supporting Information). This is in good agreement with the compositions determined from the PXRD analysis, 14.65 ± 0.08 atom% Sn and 13.5 ± 0.1 atom% Sn for the 250 and 270°C reactions, respectively. Consistent with thiol passivation, S is observed in the spectra at low concentrations, 2.2 ± 1.0 atom% and 1.5 ± 1.0 atom% for 250 and 270 °C, respectively. The spectrum obtained from EDS elemental mapping of Ge and Sn gives a similar composition, 14.4 ± 0.8 atom% Sn and 85.6 ± 1.9 atom% Ge (Figure S5 in the Supporting Information).

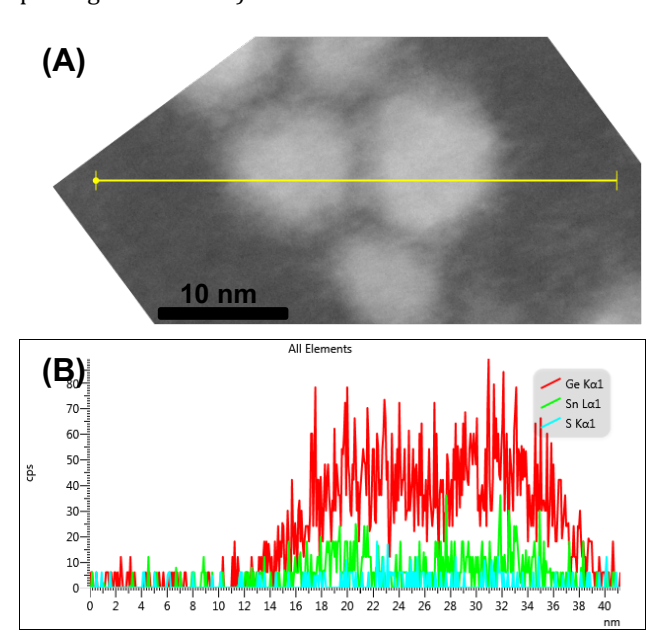


Figure 3. (A) Dark field STEM image and (B) corresponding EDS line scan of DDT-capped $Ge_{1-x}Sn_x$ NCs synthesized at 250 °C. The yellow line on the dark field stem image is the path of the line scan.

Characterization of Particle Size

Particle diameter was determined from bright field STEM images (Figure 4 and Figure S6 in the Supporting Information). Reported diameters are the geometric mean of the Feret maximum and Feret minimum diameters across approximately 500 unique NCs for each sample (Figures S7-S14 in the Supporting Information). Figure 5 shows the

dependence of particle and crystallite size on reaction temperature for both OAm-capped and DDT-capped $Ge_{1-x}Sn_x$ NCs. The crystallite diameter increases with increasing temperature, although not in a linear fashion. At the highest temperatures the slope is reduced, suggesting that concentration rather than temperature is more important for

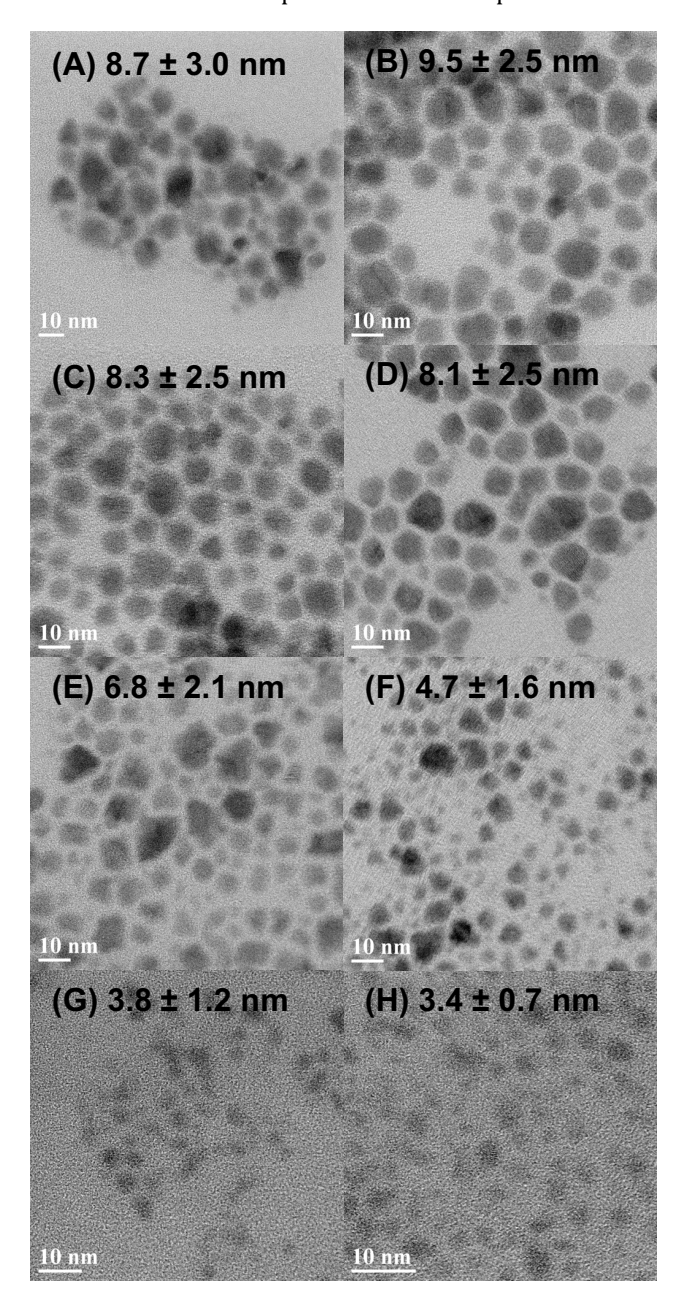


Figure 4. Bright field STEM images of DDT-capped $Ge_{1-x}Sn_x$ NCs synthesized at (A) 280, (B) 270, (C) 260, (D) 250, (E) 240, (F) 230, (G) 220, and (H) 210 °C.

controlling size at higher temperatures. Similar to the dependency of crystallite diameter on temperature, particle diameter determined from STEM images increases with synthesis temperature until 260°C, at which point the average particle diameter appears to remain constant. Small changes in particle diameter relative to the starting OAmcapped samples are observed for the DDT-capped $Ge_{1-x}Sn_x$ NCs. The percent change relative to the diameter of OAm-

capped $Ge_{1-x}Sn_x$ NCs are within 11% for most temperatures employed in synthesis. However, following ligand exchange, the 240 and 270 °C samples have decreased in size by 24% and 15%, respectively. This is attributed to the precipitation purification technique as some of the larger particles may have been inadvertently removed from the sample, thereby biasing the DDT-capped samples toward the smaller average particle size. The decrease in size can also be attributed to etching of the particle surface by hydrazine during the ligand exchange procedure.

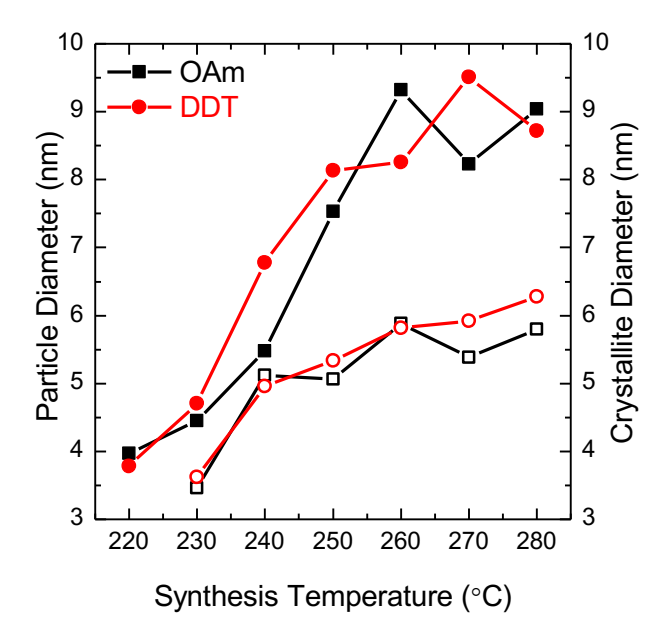


Figure 5. Particle (filled) and crystallite (open) sizes as a function of temperature for OAm- and DDT-capped $Ge_{1-x}Sn_x$ NCs.

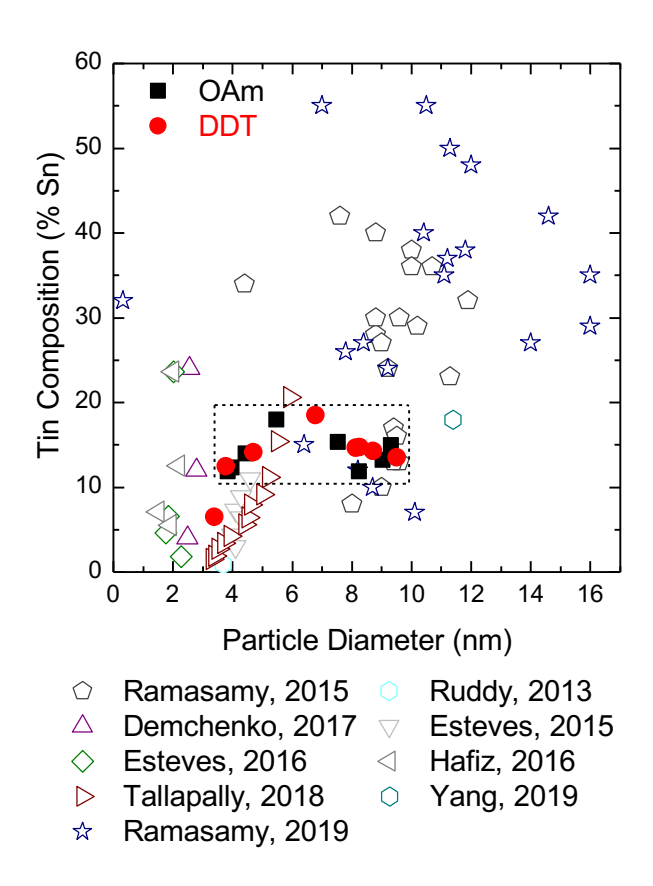


Figure 6. Sn composition as a function of particle diameter of OAm- and DDT- capped $Ge_{1-x}Sn_x$ NCs compared to those reported in the literature. (A box is outlined to highlight the samples reported herein.)

To date, literature on the synthesis and characterization of Ge_{1-x}Sn_x NCs has focused on convection heating methods to achieve a wide range of Sn compositions while controlling particle diameter. Esteves et al.,18 Hafiz et al.,16 and Demchenko et al.19 have synthesized Ge1-xSnx NCs with diameters less than 4 nm, demonstrating size control across a range of low compositions, $0.04 \le x \le 0.24$. Ramasamy et al. have demonstrated similar control for larger diameter Ge₁₋ _xSn_x NCs with larger Sn compositions.^{29,30} In this work, facile microwave heating methods are used to achieve a wide range of particle sizes, 3.8-9.3 nm in diameter, across a narrow range of Sn compositions, $0.12 \le x \le 0.18$, by varying synthesis temperature (Figure 6). Particle size is observed to change rapidly between 230 and 260 °C (Figure 5). Although Sn composition reaches a maximum of 17.9% Sn at 240 °C, it is otherwise limited to 14-15.5% Sn in this temperature regime (Figure 2).

EXAFS Characterization

EXAFS was used to study the local structure of DDT-capped Ge_{1-x}Sn_x NCs synthesized at 230, 240, and 250 °C. NC samples were synthesized for EXAFS studies, and their properties are slightly different from those given in Table 1. Due to batch variation, crystallite size is slightly smaller, and the maximum Sn composition is observed for the 230 °C sample. The crystallite diameters were determined to be 3.3(1), 4.0(1), and 4.6(2) nm by Scherrer analysis of the PXRD patterns for NCs synthesized at 230, 240, and 250 °C,

respectively (Figure S15 in the Supporting Information). The Sn compositions were determined by Rietveld refinement of the PXRD patterns and are 16.7(2), 16.2(1), 13.9(1)% Sn for NCs synthesized at 230, 240, and 250 °C, respectively (Figure S16 and Table S2 in the Supporting Information). FTIR spectroscopy confirms the DDT surface passivation (Figure S17 in the Supporting Information). UV-Vis-NIR spectroscopy confirms an indirect bandgap that decreases with increasing particle size (Figure S18 in the Supporting Information).

Ge and Sn K edge spectra were collected at 10 K, and the data were fit in r-space as the sum of theoretical pair functions calculated from a Ge diamond cubic crystal structure using FEFF7.⁴⁴ Data were also collected for bulk and pure Ge NCs and were used to estimate the amplitude reduction factor, S_o^2 , for Ge. Fits yielded S_o^2 values between 1.0 and 1.04, with slightly more broadening for the NCs; an average S_o^2 of 1.02 was used for the Ge edge fits. For the Sn K edge, an average over all samples gave an S_o^2 of 1.07.

The distances, r, between pairs of atoms was calculated for a $Ge_{1-x}Sn_x$ diamond cubic crystal, using an expanded lattice constant that was estimated from Vegard's law for a structure with x = 0.15. The calculated pair distances served as the starting point for fitting the pair functions (Table S3 in the Supporting Information). The initial Sn-Ge, Ge-Sn, and Sn-Sn functions were determined by substituting one or two Sn atoms on an undistorted Ge lattice site; the starting pair distances are those of the diamond cubic lattice for the x = 0.15 alloy. The distribution of fitted distances for each pair is described as a Gaussian distribution with width and amplitude given by σ and N, respectively; the amplitude, N, gives the coordination number (the number of neighboring atoms in each shell). Disorder is inferred from the Debye-Waller factor, σ^2 , which is calculated from the peak width, σ

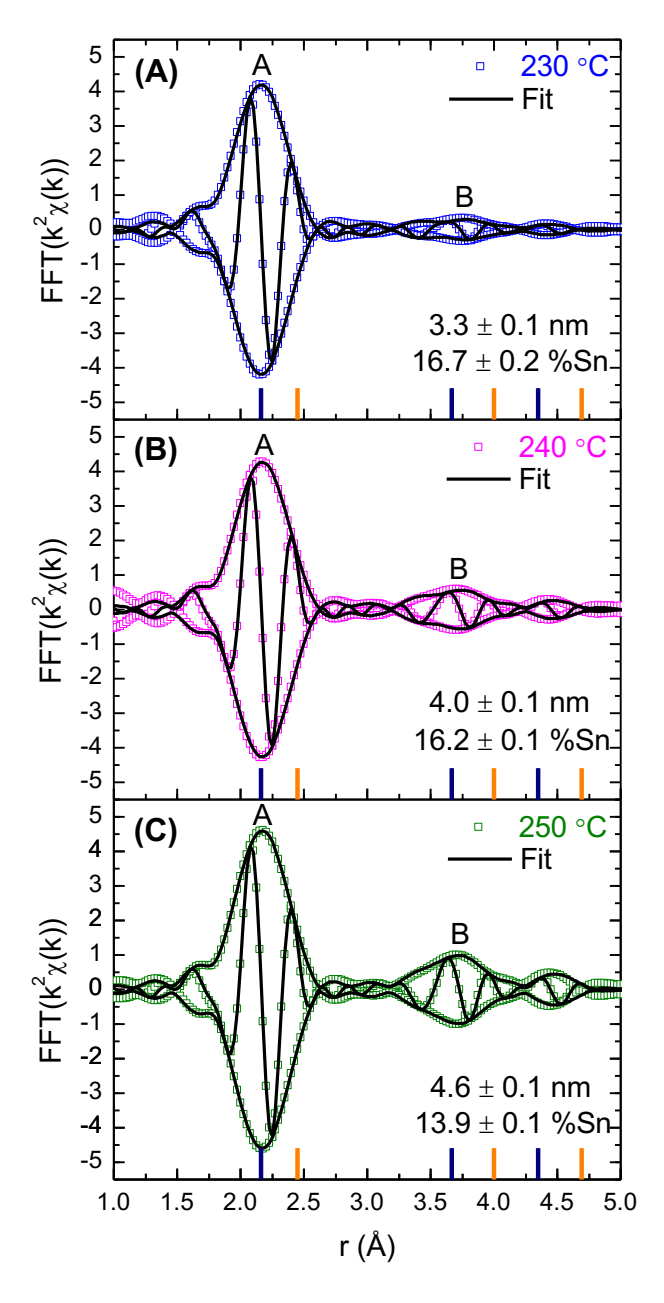


Figure 7. Fast Fourier k^2 -weighted transforms of the Ge K edge data (open squares) and r-space fits (black line) for the DDT-capped $Ge_{1-x}Sn_x$ NCs synthesized at (A) 230, (B) 240, and (C) 250 °C. Crystallite size and Sn composition are provided for each spectrum. Bars on the x-axis show pair distances obtained from diffraction (orange bars) and the expected Ge-Ge EXAFS peak positions for an undistorted Ge lattice (dark blue bars). The FT range is 3.5-14.5 Å-1 and the fit range in r is 1.7-4.8 Å. Here and in other EXAFS plots, the fast oscillating function is the real part R of the FT and the amplitude function is $(R^2 + I^2)^{1/2}$, where I is the imaginary part of the FT.

The k-space EXAFS data are given in Figure S19 in the Supporting Information, and the r-space EXAFS data and fits are shown in Figures 7 and 8 for Ge and Sn K edges, respectively. The fitting results are summarized in Table 2. Each Ge edge spectrum exhibits first and second nearest neighbor (NN) peaks near 2.16 and 3.7 Å, which are labeled A and

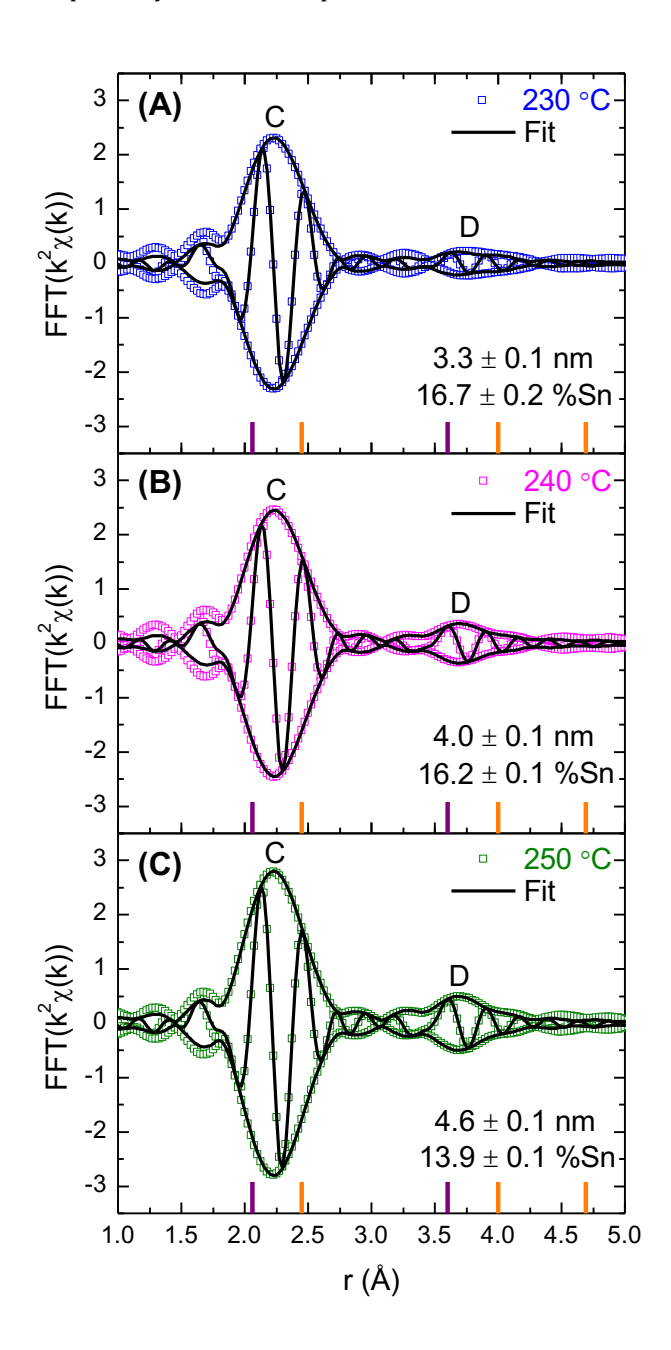


Figure 8. Fast Fourier k²-weighted transforms of the Sn K edge EXAFS data (open squares) and r-space fits (black line) for the DDT-capped Ge_{1-x}Sn_x NCs synthesized at (A) 230, (B) 240, and (C) 250 °C. Crystallite size and Sn composition are provided for each spectrum. Bars on the x-axis show pair distances obtained from diffraction (orange bars) and the expected Sn-Ge EXAFS peak positions for an undistorted Ge lattice (purple bars). The FT range is 3.5-13.5 Å-¹ and the fit range in *r* is 1.8-4.2 Å.

small to reliably fit. Peak A is modeled as a combination of the Ge-Ge first NN and Ge-Sn first NN paths; the latter is a small peak (Figure S20 in the Supporting Information). Peak B is modeled as the Ge-Ge second NN path but with a small amplitude. Fits were also carried out including a small Ge-Sn second NN peak, but this peak is very small and could not be fit reliably. For the Sn K edge data, each EXAFS spectrum exhibits peaks near 2.2 and 3.7 Å, which are labelled C and D, respectively. Peak C is modeled as a combination of the Sn-Ge first NN and Sn-Sn first NN paths. Peak D is modeled

Table 2. Pair distances (r), Debye-Waller Disorder Factors (σ^2), and Coordination Numbers (Λ) from Fits to the Ge and Sn K Edge EXAFS Spectra of Ge_{1-x}Sn_x NCs Synthesized at 230, 240, or 250 °C.^{a,b}

Ge K Edge									
Path	230 °C			240 °C			250 °C		
	r (Å)	σ² (Ų)	N	<i>r</i> (Å)	σ² (Ų)	N	<i>r</i> (Å)	σ² (Ų)	N
Ge-Ge (1st NN)	2.457(5)	0.0038(4)	3.8	2.459(5)	0.0035(4)	3.7	2.458(5)	0.0031(4)	3.7
Ge-Sn (1st NN)	2.615(10)	0.003(1)	0.2	2.618(10)	0.0027(6)	0.3	2.623(10)	0.0020(5)	0.3
Ge-Ge (2 nd NN)	4.07(3)	0.0087(9)	2	4.06(2)	0.0068(9)	4	4.04(2)	0.0061(6)	7
Sn K Edge									
Path	230 °C		240 °C			250 °C			

	r	σ^2	N	r	σ^2	N	r	σ^2	N
	(Å)	(Ų)		(Å)	(Ų)		(Å)	(Ų)	
Sn-Ge (1st NN)	2.61(2)	0.0038(10)	3.4	2.60(2)	0.0044(10)	3.6	2.59(2)	0.0035(10)	3.6
Sn-Sn (1st NN)	2.74(2)	0.009(1)	0.6	2.74(2)	0.0020(5)	0.4	2.73(2)	0.0020(5)	0.4
Sn-Ge (2 nd NN)				4.03(3)	0.0025(5)	2	4.04(3)	0.0022(5)	3

^a The first atom listed in each pair gives the relevant edge spectra.

^b The errors on the coordination numbers are approximately 15% for the large peaks (Ge-Ge and Sn-Ge) because of correlations between N and σ^2 . The errors on the small peaks (Ge-Sn and Sn-Sn) are larger, approximately 30%. The errors on the second NNs are + 1.

as the Sn-Ge second NN path. When spectra were modeled including Sn-O and Ge-O first NN paths, the oxide peak amplitudes went to zero, suggesting low levels of Ge and Sn oxidation. Both the Sn and Ge edges were fit with contributions from Sn-S and Ge-S paths to investigate whether contributions from the DDT ligands could be observed, but these paths did not make a significant contribution to the observed spectra.

For the second NN shell only the main contribution is reported: the Ge-Ge pair for the Ge edge and the Sn-Ge pair for the Sn edge. The errors on the pair distances are larger, depending in part on whether the small contributions from Ge-Sn or Sn-Sn were included in the fit. Surprisingly, the Ge-Ge and Sn-Ge distances are essentially the same, 4.04-4.07 Å for Ge-Ge and 4.03-4.04 Å for Sn-Ge. These results are in good agreement with the average second NN distances in GeSn alloy films, 4.05 Å. 52 While the second NN Ge-Ge and Sn-Ge distances are essentially the same, the first shell bond lengths are quite different; this suggests that the larger size of the Sn atom is mainly accommodated by local bond bending. The pair distances are consistent with Sn substituting on the Ge position in the diamond cubic crystal structure and provide further support for an alloy structure.

In a diamond cubic lattice structure, the maximum coordination number for a central atom is 4 atoms in the first NN shell and 12 atoms in the second NN shell. The expected coordination by a given element, N_R , in the first and second NN sites depends on composition and is calculated for a random distribution using the relationship given in Equation 2,

Equation 2.
$$N_R = \frac{n!}{x!(n-x)!} p^x (1-p)^{n-x}$$

in which n is the number of NN sites, x is the number of sites occupied by a given element, and p is the composition of the element in the sample (Table S4 in the Supporting Information). For 15% Sn, 3.4 Ge-Ge pairs and 0.6 Ge-Sn pairs are expected in the first NN shell. The coordination numbers for the large first NN peaks vary from 3.7 to 3.8 for Ge-Ge and from 3.4 to 3.6 for Sn-Ge. These are slightly larger than expected but are within the 15% uncertainty. The coordination numbers for the small first NN peaks are correspondingly low, 0.2-0.3 for Ge-Sn and 0.4-0.6 for Sn-Sn, compared to the expected value of 0.6 but are consistent within the larger uncertainty for these peaks. Also, the small coordination numbers for the Sn-Sn NN peaks indicate that very little Sn clustering has occurred; if a significant number of Sn clusters were present, the number of NN Sn atoms would be large. Although the Ge-Sn and Sn-Sn first NN peaks are small, they are significant based on the Hamilton F-test, and the fits with these peaks removed are significantly worse.53

These fits suggest that the Sn concentration within the NCs may be lower than the average measured concentrations, which may indicate higher Sn incorporation at the NC surface.

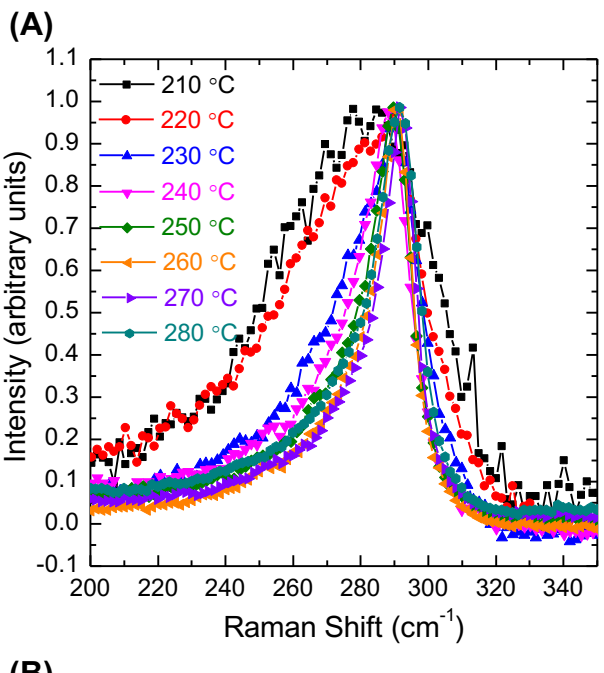
The second NN peaks are smaller for both edges compared to those of pure Ge NCs, which indicates significant disorder beyond the first NNs.²² The disorder is the smallest for the sample prepared at 250 °C, which has the largest second NN peaks. From our studies of similarly-prepared undoped Ge NC reference samples,²² the extracted second NN coordination numbers were between 6 and 9 for NCs in the 3-9 nm range; these coordination numbers suggest that the NCs are composed of 2-3 smaller crystallites. Similar Ge second NN coordination numbers are expected for the Ge_{1-x}Sn_x NC samples. For the Ge K edge, the fits yield 2-7 second NN Ge atoms in each sample with a large broadening, and the coordination number is highest for the 250 °C sample. For the Sn edge, the number of second NNs is much smaller, 2-3 second NN Ge atoms in each sample. Note that for a lattice with significant distortions, EXAFS preferentially sees the more ordered regions. If the distribution of second neighbors is described by a sum of two Gaussians, one relatively narrow and the other broad, then the broad peak is often not observed. Here, σ^2 is relatively small for the Sn-Ge second NN peak so contributions from a broad peak may not be observable. Thus, the local structure beyond the first NN shell becomes disordered quickly. The third NN peak is very small, even for the Ge edge data, and the environment surrounding a Sn atom is significantly more disordered than around a Ge atom. Incorporation of a significant fraction of Sn into the surface layer could also lead to decreased second NN coordination. However, the large size of the first NN peak, attributable to a large number of Ge-Ge and Sn-Ge pairs, indicates that this is not a major effect.

Small σ^2 values ($\sigma^2 \le 0.010 \text{ Å}^2$) are observed for the first NN peaks for both the Ge and Sn edge data, providing support for a fairly well-ordered structure. Observation of the Ge-Ge and Sn-Ge 2nd NN peaks also indicates the presence of long-range order.54,55 The observed values of σ^2 for the Ge-Ge first NN peaks, 0.003-0.004 Å² are similar to but slightly smaller than those of comparably sized reference cubic Ge NCs (~ 0.0026 -0.0029 Å²) measured at 10K.⁵⁶ This indicates that alloying with Sn introduces more disorder than is observed in similarly sized Ge NCs. The σ^2 values for the Ge-Ge second NN peaks are quite large, again indicating significant disorder beyond the first neighbor shell, but are similar to those of reference cubic Ge.55,57 In contrast, σ^2 values for the Ge-Sn second NN peaks are small. As noted above the combination of a small number of second NNs and a small value of σ^2 suggests that the Ge-Sn second NN distribution may be bimodal with a small sharper peak and a larger very broad peak. However, the amplitude is too small to fit such a distribution.

Raman Spectroscopy

Raman spectra were collected for OAm- and DDT- capped Ge_{1-x}Sn_x NCs and provide further support for the formation of nanoscale alloy structures (Figure 9 and Figures S21-S22 in the Supporting Information). The Ge-Ge optical phonon mode, expected at 300 cm⁻¹ in bulk Ge, is observed as a broadened peak near 290 cm⁻¹, which is consistent with Sn incorporation. There is no evidence for amorphous Ge (154 cm⁻¹ and 275-280 cm⁻¹), GeO₂ (440 cm⁻¹, 550, and 880 cm⁻¹), β-Sn (125 cm⁻¹), nor SnO₂ (640 cm⁻¹).^{17, 58-62} A weak peak is observed near 175 cm⁻¹and may be assigned to the Sn-Sn mode of α-Sn, which is expected at 197 cm⁻¹.63,64 However, the Ge longitudinal acoustic phonon modes are also expected near 175 cm⁻¹ so this peak is better understood as a mixture of Sn-Sn optical and Ge longitudinal acoustic modes. 63, 64 Absence of an explicit Sn-Sn mode suggests no phase segregation or Sn clustering in the Ge_{1-x}Sn_x NCs, in agreement with the EXAFS results.

The Ge-Ge(Sn) optical phonon mode of the $Ge_{1-x}Sn_x$ NCs is observed as a broadened, asymmetric peak that is shifted from the expected position for bulk Ge. Quantum confinement , alloy disorder, amorphousness, and surface effects can contribute to peak shifting and broadening in Raman spectra. To quantify broadening and peak shift, the spectra were fit as the sum of two Lorentzian terms and a linear baseline function given by Equation 3,



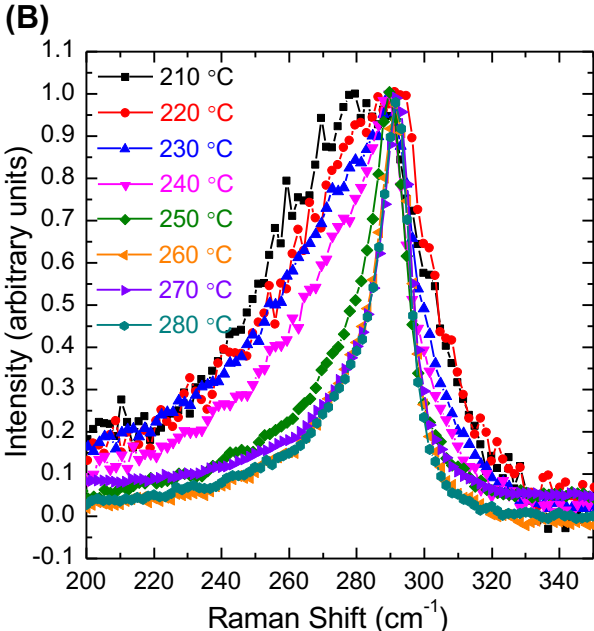
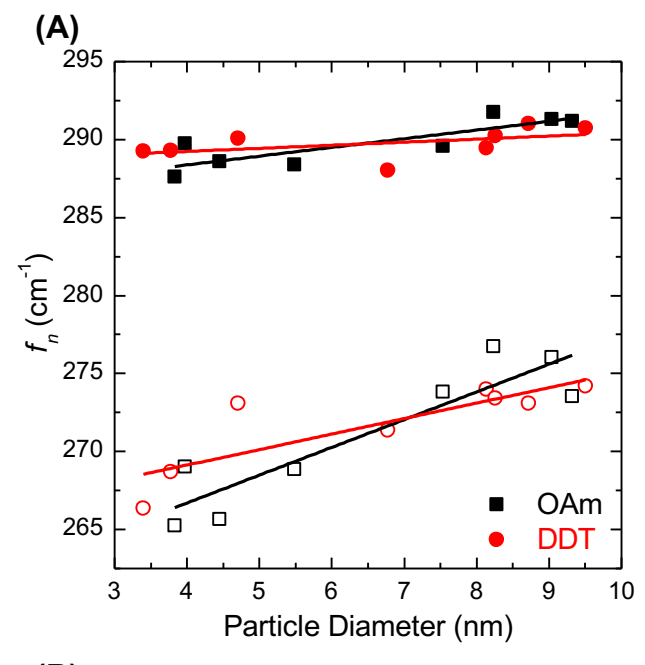


Figure 9. Raman spectra of (A) OAm- and (B) DDT-capped $Ge_{1-x}Sn_x$ NCs synthesized at the indicated temperatures, normalized and magnified to show the shifting of the Ge-Ge phonon mode.

Equation 3.

$$F(x) = \frac{A_1 \Delta f_1^2}{4[(f_1 - x)^2 + \left(\frac{\Delta f_1}{2}\right)^2]} + \frac{A_2 \Delta f_2^2}{4[(f_2 - x)^2 + \left(\frac{\Delta f_2}{2}\right)^2]} + mx + b$$

where A_n is the peak intensity, Δf_n is the full width at half maximum, f_n is the peak center, x is the Raman shift, m is the slope of the baseline and b is the y-intercept of the baseline. Background intensity off-set is compensated for by the linear baseline function given by mx + b (Figures S23-S24 in the Supporting Information). ^{46,68-71} The higher frequency Lorentzian term fits the Ge-Ge(Sn) optical phonon mode,



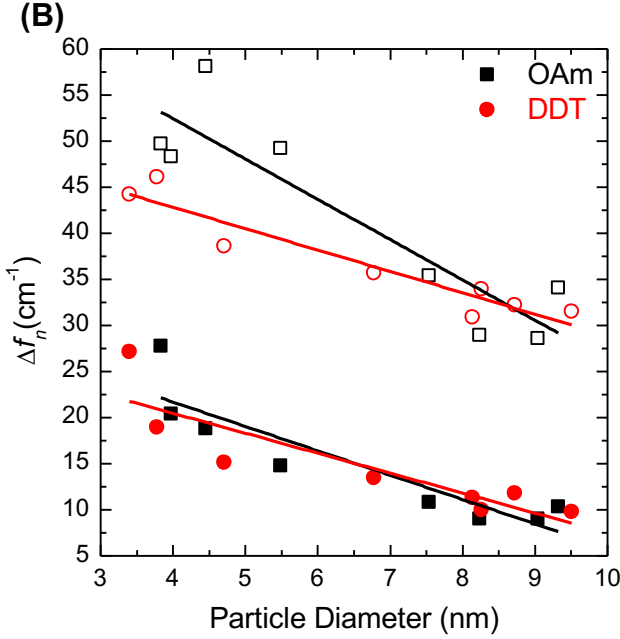


Figure 10. (A) Raman peak shift (f_n) and (B) full-width at half maximum (Δf_n) of the Ge-Ge(Sn) optical phonon mode (filled) and shoulder (open) peaks for OAm- (black squares) and DDT (red circles) -capped Ge_{1-x}Sn_x NCs synthesized at 210-280 °C.

and the lower frequency Lorentzian term accounts for peak asymmetry due to disorder, quantum confinement, and surface effects. The results of fitting are summarized in Table S4 in the Supporting Information. The Raman shift of the Ge-Ge(Sn) optical phonon mode and the asymmetry term increase with particle diameter for OAm- and DDT- capped $Ge_{1-x}Sn_x$ NCs synthesized at 210-280 °C (Figure 10). The full width at half maximum values decrease as particle size increases. These results are consistent with crystallinity increasing as a function of particle size and with the phonon confinement model previously described for Ge NCs. 46 , 66 , 72 , 73 The $Ge_{1-x}Sn_x$ NCs demonstrate a greater degree of peak

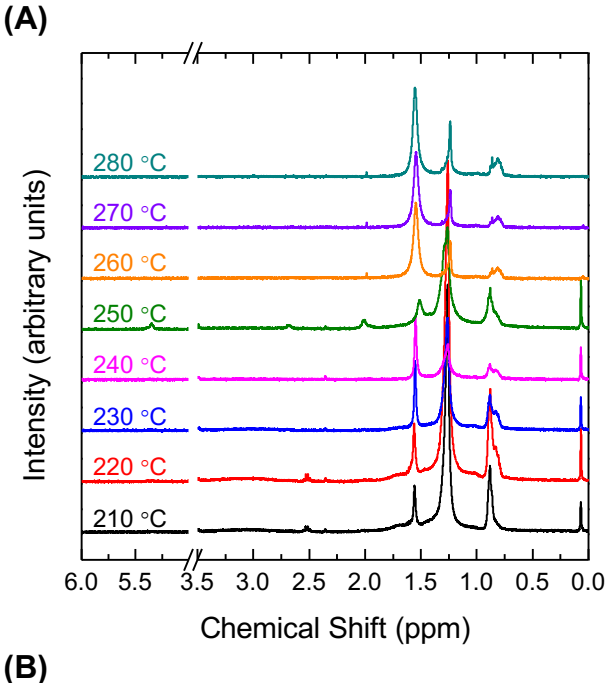
shifting and broadening than was previously reported for Ge NCs synthesized by the microwave-assisted reduction of GeI₂ with the addition of GeI₄, I₂, or Br₂ to control particle size. ⁴⁶ The additional peak shifting and broadening are consistent with alloying. For Sn compositions less than 10%, the effect of alloy disorder on the Ge-Ge optical phonon mode has been shown to be linearly dependent on the Sn composition for Ge_{1-x}Sn_x thin films. ^{4, 5, 74, 75} Outside this composition regime, however, the effects of nanoscaling and alloying cannot be deconvoluted without additional studies in which size, strain, and Sn composition are systematically controlled. ⁷⁶⁻⁷⁹

Characterization of the Nanocrystal Surface

 ^1H NMR spectroscopy was used to confirm the presence of OAm as a passivating ligand on the surface of the as-made Ge_1-xSn_x NCs (Figure S25 in the Supporting Information). The vinylic and allylic proton peaks, characteristic of the C=C double bond in OAm, are observed at 5.33 and 1.96 ppm, respectively. $^{32, \, 80, \, 81}$ Alkyl and terminal methyl proton peaks are observed at 1.24 and 0.86 ppm, respectively. The α -protons, which are expected at 2.6 ppm and are deshielded by the terminal amine group in free OAm, are observed to be shifted down field between 2.8 ppm and 3.0 ppm for the OAm-capped Ge_1-xSn_x NCs. The chemical shift from the amine proton, expected at 1.05 ppm, is not observed. The absence may be attributed to peak broadening due to close proximity of the NC surface or rapid exchange of the acidic proton. $^{34, \, 82-84}$

Following ligand exchange, the surface of DDT-capped Ge_{1-x}Sn_x NCs were characterized by ¹H NMR spectroscopy, and the spectra were compared to that of unbound DDT (Figure 11 and Figures S26-S27 and Table S5 in the Supporting Information). Peaks near 1.25 ppm and 0.88 ppm correspond to the alkyl and terminal methyl groups, respectively. These peaks are found in similar positions in OAmcapped nanocrystals and are not diagnostic. DDT can be distinguished from OAm by chemical shifts originating from the α - and β -protons, which are deshielded by the terminal thiol group. These peaks are observed at 2.52 and 1.55 ppm, shifted downfield from their expected positions at 2.36 and 1.46 ppm for the α- and β-protons, respectively.85 Following ligand exchange, it is expected that peaks originating from the vinylic and allylic protons of OAm will be lost. For most syntheses, the vinylic and allylic peaks are not observed for the DDT-capped Ge_{1-x}Sn_x NCs, confirming a complete exchange of OAm for DDT ligands.32 However, weak vinylic and allylic peaks are observed for Ge_{1-x}Sn_x NCs synthesized at 250 °C and recapped at 150 °C (Figure S27 in the Supporting Information). Although 90 minutes is enough sonication time for most hydrazine treatments, there is batch variation, and sonication time should be extended until a totally clear solution is obtained following centrifugation. In additional ligand exchange experiments, Ge1-xSnx NCs were recapped with DDT by microwave-assisted heating at 100 °C for 1 h or by stirring at room temperature for 24 h. Vinylic and allylic peaks were observed for samples synthesized at 240 °C and recapped at 100 °C but were not observed for any samples that were recapped at room temperature by stirring for 24 hours (Figure S27 in the Supporting Information). This suggests that as synthesis temperature increases, the amine ligand binds more strongly to the

nanocrystal surface, and higher temperatures or longer reaction times for the hydrazine treatment/ligand replacement reaction are necessary for the thiol to completely replace the amine at the nanocrystal surface.



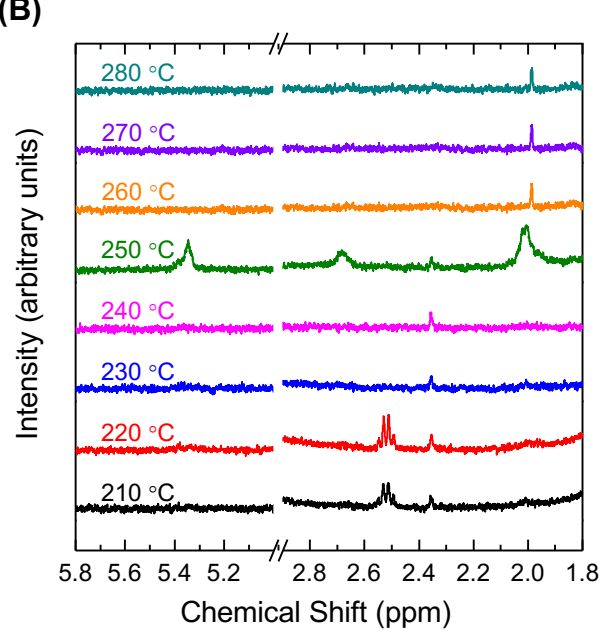


Figure 11. ¹H NMR spectra of $Ge_{1-x}Sn_x$ NCs recapped with DDT by heating at (A) 150 °C for 1 hour and (B) a magnified view to show the vinylic and allylic protons at 5.33 and 1.96 ppm, respectively.

FTIR spectroscopy was used to further characterize the $Ge_{1-x}Sn_x$ NC surface before and after ligand exchange. The spectra of the $Ge_{1-x}Sn_x$ NCs prior to ligand exchange show the vinylic C-H stretch at 3005 cm⁻¹, a C=C stretch near 1630 cm⁻¹, and an NH₂ bend at 1525 cm⁻¹, consistent with OAm passivation.⁸⁶ (Figure S28 in the Supporting Information). The small peak at 965 cm⁻¹ is consistent with a trans C=C

bend and suggests that some of the ligand converts from the *cis*- to the *trans*- isomer during the reaction. ^{86, 87} The amine N-H stretch, which is characteristic of OAm on the NC surface, is observed as a broad peak above 3000 cm⁻¹. A Ge-N stretch, expected between 600 cm⁻¹ and 800 cm⁻¹, is not explicitly observed, and the Sn-N vibration occurs outside the collectable range of available instrumentation. ⁸⁸ A broad peak is observed from 500-900 cm⁻¹ and is attributed to oxidation that occurred during the spectrum collection. The broad peak may include contributions from Ge-OH, Ge-O, Ge-O-Ge, and Ge-N stretching vibrations. ⁸⁹⁻⁹² The broad peak may also include contributions from Sn-O and Sn-O-Sn stretching modes. ⁹³⁻⁹⁷

Following ligand exchange, FTIR spectra verify the replacement of OAm with DDT ligand (Figure 12). The loss of peaks at 3005 cm⁻¹, 1630 cm⁻¹, and 1525 cm⁻¹ confirm OAm is no longer present at the NC surface. The loss of the amine stretch near 3300 cm⁻¹ provides further support for full ligand replacement. Peaks consistent with an alkyl chain are observed at 2852 cm⁻¹, 2922 cm⁻¹, and 2955 cm⁻¹, and an additional peak indicative of conformational ordering of neighboring chains is observed at 1300 cm⁻¹.98 The characteristic C-S and S-H stretching peaks, expected near 720 cm⁻ ¹ and 2550-2600 cm⁻¹, respectively, are not observed, likely due to weak intensities overall. 32, 33, 99, 100 The Ge-S and Sn-S vibrations are expected near 375 cm⁻¹, which is at the edge of the collectable range of available instrumentation, and are not observed. 101, 102 Oxidation peaks are not observed for the DDT-capped Ge_{1-x}Sn_x NCs, indicating that improved surface passivation is achieved via ligand exchange. Consistent results were obtained for Ge_{1-x}Sn_x NCs passivated with DDT by stirring at room temperature for 24 hours and by microwave-assisted heating at 100 °C for 1 hour (Figure S29 in the Supporting Information).

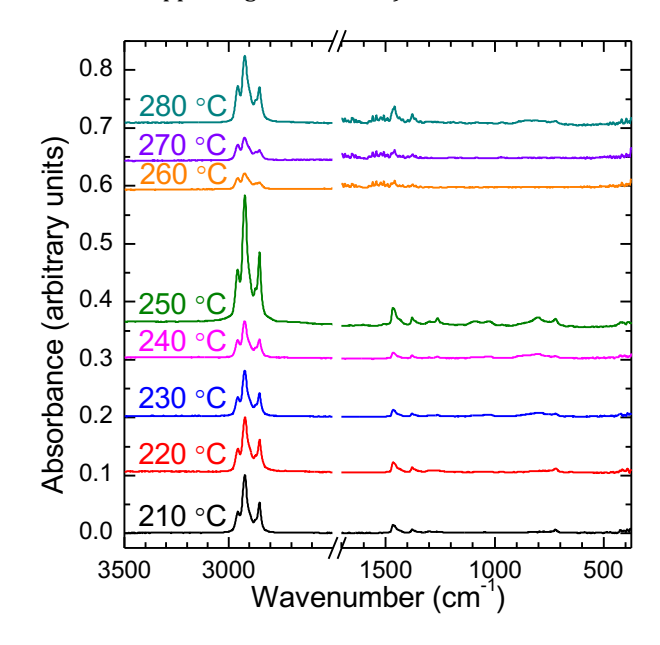


Figure 12. FTIR spectra of DDT-capped $Ge_{1-x}Sn_x$ NCs.

Characterization of Optical Properties

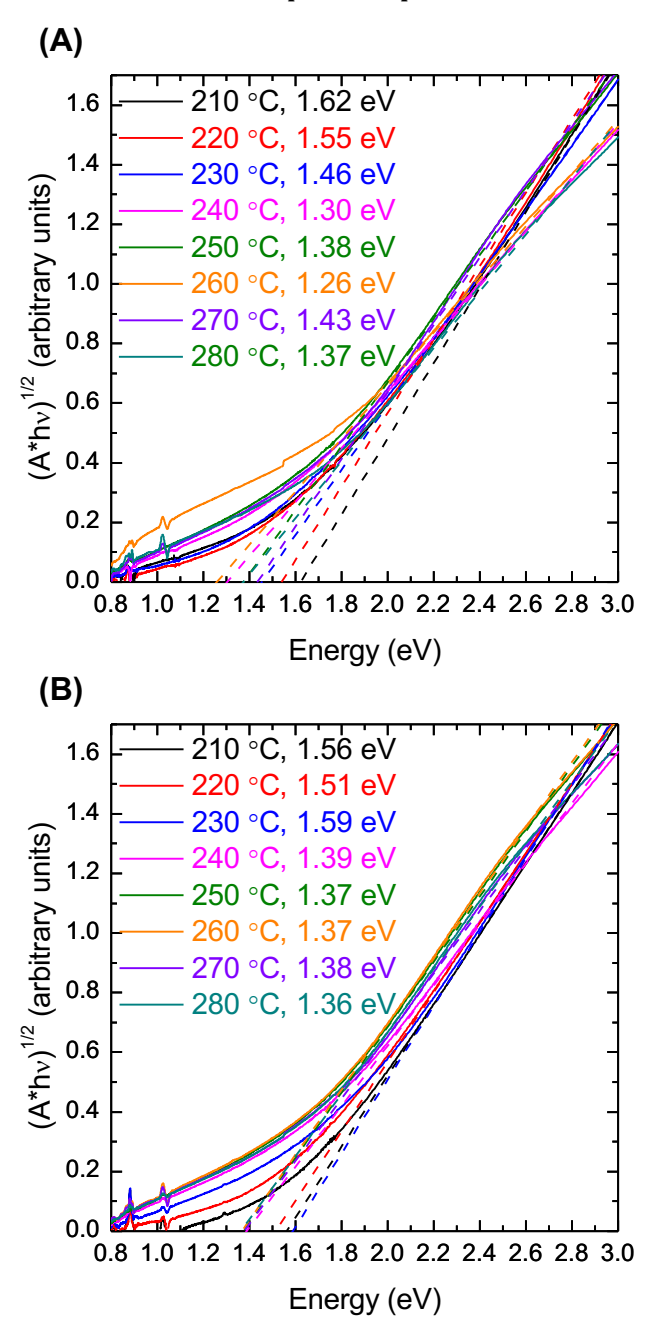


Figure 13. Tauc plots for indirect band gap of $Ge_{1-x}Sn_x$ NCs synthesized at the indicated temperatures and passivated with (A) OAm and (B) DDT.

Optical absorption spectroscopy was performed on dilute solutions of $Ge_{1-x}Sn_x$ NCs to determine the band gap energy of the material (Figure S30 in the Supporting Information). Ge NCs are known to be indirect band gap absorbers, and theory predicts that an indirect to direct band gap crossover will occur at $0.06 \le x \le 0.11$ for $Ge_{1-x}Sn_x$ NCs. Determination of band gap from direct band gap Tauc plots gives larger band gap values than those determined from indirect Tauc plots; thus, optical data do not suggest indirect-to-direct band gap crossover has occurred. This is likely due to Sn compositions below the point of crossover and is consistent with results for $Ge_{1-x}Sn_x$ NCs reported in the current

literature. Indirect band gap Tauc plots for the samples are provided in Figure 13. The indirect band gap, Eg, was calculated as the x-intercept of a line tangent to the experimental curve. The indirect band gap is observed to decrease with increasing synthesis temperature (Figure 14). Due to quantum confinement, the indirect band gap also decreases as particle size increases up to 7 nm, at which point it plateaus. For larger particles, the observed band gap does not change with size as expected based on the observed change in average particle diameter but is consistent with a polydisperse sample. Absorbance at higher energies by smaller diameter particles in these samples shifts the band gap of the ensemble toward higher energies. Following ligand exchange, the band gap energies of some DDT- capped samples are increased relative to those of the OAm-capped NCs while others are decreased. There is not a consistent trend in how the band gap energy changes following ligand exchange. Variations at the particle surface due to differences in size and composition of the NCs causes the surfaces to be differently affected by ligand exchange.

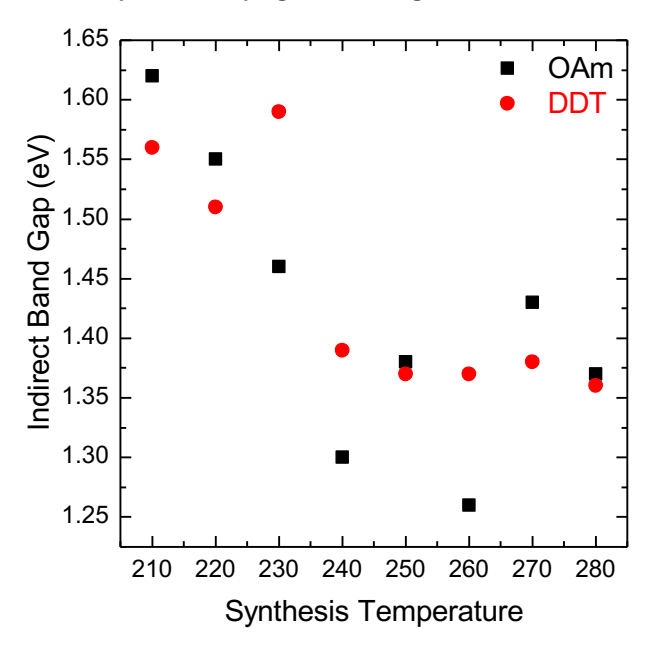


Figure 14. Indirect band gap energy (eV) as a function of synthesis temperature for OAm- and DDT- capped $Ge_{1-x}Sn_x$ NCs.

The absorption onset of Ge and Ge1-xSnx NCs has been reported in the literature from optical absorbance and diffuse reflectance spectroscopies. While most groups use a Tauc plot analysis in which the band gap is determined as the xintercept of an extrapolated tangent line, methods of selection of the linear region and extrapolation vary. Ruddy et al. select the linear region based on absorbance, linearly fitting the region in which absorbance is 0.05-0.15 for data normalized at 400 nm.²⁸ Esteves et al. report performing multiple linear regression fittings, with the difference in bounds ranging from 0.3 to 0.6 eV and selecting the fit with the greatest R².¹⁷ Ramasamy noted that multiple linear regions may be identified, depending on the magnification of a Tauc plot for direct band gap analysis.²⁹ Tauc plots for indirect band gap analysis may also have curvature, which contributes to ambiguity in the extrapolation of the plot's linear region.

Linear fittings were also performed in order to compare the method reported herein to those in the literature. For the OAm-capped Ge_{1-x}Sn_x NCs synthesized at 250 °C, Tauc plots were constructed with absorbance data normalized at 400 nm. Then, multiple linear regressions were performed with the difference in the bounds ranging from 0.1 to 1.0 eV (Table S6 in the Supporting Information). Multiple fits were performed for each range, shifting the bounds by 0.1 eV for each fitting. The fit with the greatest slope and R² value for each range was identified to give the band gap. The maximum slope and R² belonged to the same fit for each range. Across the series, the band gap decreases from 1.40 eV to 1.35 eV as the difference in the bounds increases. All fit ranges are overlapping. The band gap obtained from the polynomial fitting method is equal to the average band gap from the linear fittings for the OAm-capped Ge_{1-x}Sn_x NCs synthesized at 250 °C, suggesting a reasonable comparison can be made between values obtained from the different methods. Experimental band gap energies, determined using a polynomial fitting, agree well with literature values for Ge_{1-x}Sn_x NCs in the 1 to 5 nm range (Figure 15). 16-19, 24, 28 However, few values have been reported for $Ge_{1-x}Sn_x$ NCs in the 5 to 9 nm range.24,29,30

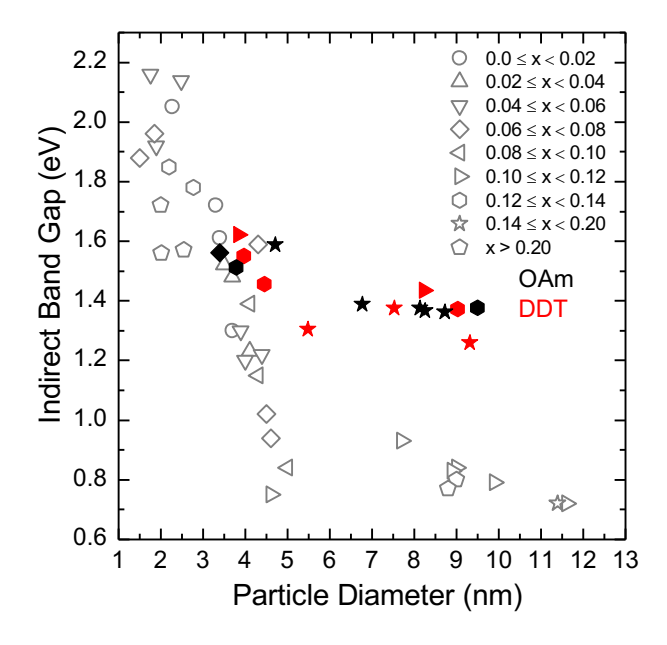


Figure 15. Indirect band gap energy (eV) as a function of particle diameter for varying Sn compositions, x, reported in in the literature (gray, open) and compared to experimental values for OAm- (black, filled) and DDT- (red, filled) capped $Ge_{1-x}Sn_x$ NCs synthesized at 210-280 °C.16-19, 24, 29, 30

CONCLUSIONS

 $Ge_{1-x}Sn_x$ NCs are of interest in the recent literature for their predicted indirect-to-direct band gap crossover. The convection-heated synthesis of this metastable material and its optoelectronic properties have been well-studied, but the predicted crossover has not been observed. In this work, microwave-assisted heating methods have been applied to the synthesis of $Ge_{1-x}Sn_x$ NCs, and the effect of temperature on particle size, composition, and structure is demonstrated. It is shown that the NC diameter increases

with synthesis temperature, while Sn composition is controlled across the range of reaction temperatures, 210-280 °C. To gain new surface functionality, which is known to influence band structure, Ge_{1-x}Sn_x NCs were treated with hydrazine to remove the OAm ligand and were then heated with DDT to achieve thiol passivation. This procedure results in a complete ligand exchange without loss of Sn composition across the synthesis temperature series. EXAFS studies of the DDT-capped Ge_{1-x}Sn_x NCs provide structural insight into this material. EXAFS confirms the alloy is a solid solution with Sn incorporation in diamond cubic lattice sites. EXAFS also shows that order increases with synthesis temperature. Raman spectroscopy further supports an alloy structure and that crystallinity increases as a function of reaction temperature and particle size. Optical spectroscopy of the OAm- and DDT-capped Ge_{1-x}Sn_x NCs confirms that due to quantum confinement, the indirect band gap energy decreases as particle size and synthesis temperature increase. Indirect-to-direct crossover is not achieved for Ge_{1-x}Sn_x NCs, but indirect band gap values are larger than those of similarly sized Ge NCs reported in the literature. 16-19, 24, 28-30 Greater control over size dispersity, composition, and surface defects, which also influence band structure, remains necessary to achieve the desired indirect-to-direct crossover. Recently, sulfide passivation of Ge and Bi-doped Ge NCs was achieved by a direct ligand exchange procedure. Sulfide passivation improved film conductivity, allowing the measurement of transport properties.²² Similar methods could be used to achieve sulfide passivation of Ge_{1-x}Sn_x NCs for incorporation in photovoltaic devices. The results presented here indicate that increased synthesis temperatures reduce structural disorder, but additional studies remain necessary to understand the role of precursor concentration and to determine a facile route to Ge1-xSnx NCs with controlled size and limited size dispersity across the full range of Sn compositions.

AUTHOR INFORMATION

Corresponding Author

* Email: smkauzlarich@ucdavis.edu

Author Contributions

The manuscript was written through contributions of all authors. All authors have given approval to the final version of the manuscript.

Notes

The authors declare no competing financial interest.

ASSOCIATED CONTENT

The Supporting Information is available free of charge on the ACS Publications website.

PXRD pattern of OAm-capped $Ge_{1-x}Sn_x$ NCs precipitated one time; Rietveld refined PXRD patterns and refinement parameters for OAm- and DDT- capped $Ge_{1-x}Sn_x$ NCs; STEM-EDS linescans, spectra, and maps for DDT- capped $Ge_{1-x}Sn_x$ NCs; STEM images and size analysis for OAm- and DDT- capped $Ge_{1-x}Sn_x$ NCs; PXRD patterns, Rietveld refined PXRD patterns and refinement parameters, FTIR spectra, and UV-vis-NIR spectra and Tauc plots for EXAFS samples; theoretical pair distances for EXAFS analysis; k-space EXAFS data; r-space EXAFS data for the Ge-Ge and Ge-Sn paths; Raman spectra , fitted spectra, and fit parameters

for OAm- and DDT- capped $Ge_{1-x}Sn_x$ NCs; ¹H NMR spectra for OAm- capped $Ge_{1-x}Sn_x$ NCs, DDT, and DDT- capped $Ge_{1-x}Sn_x$ NCs repassivated in varied conditions; FTIR spectra for OAm- and DDT- capped $Ge_{1-x}Sn_x$ NCs; UV-vis-NIR spectra for OAm- and DDT- capped $Ge_{1-x}Sn_x$ NCs; a summary of linear fitting of Tauc plots.

ACKNOWLEDGMENT

This work was supported by the National Science Foundation (CHE-1710110) and the Graduate Assistance in Areas of National Need (GAANN) Fellowship (P200A120187). EXAFS experiments were performed at the Stanford Synchrotron Radiation Lightsource (SSRL), which is supported by the U.S. Department of Energy, Office of Science, Office of Basic Energy Sciences under Contract No. DE-AC02-76SF00515. The authors are grateful to the Advanced Material Characterization and Testing Lab (AMCaT) in the UC Davis Department of Materials Science and Engineering, the Keck Spectral Imaging Facility in the Nanomaterials in the Environment, Agriculture and Technology Organized Research Unit (NEAT ORU) in the UC Davis Department of Chemistry, and the UC Davis Nuclear Magnetic Resonance Facility in the UC Davis Department of Chemistry for access to the STEM-EDS, Raman, and NMR instrumentation. The authors thank Dr. Kristie Koski (Department of Chemistry, UC Davis) for assistance with the analysis of Raman spectra and Christopher Perez (Department of Chemistry, UC Davis) for assistance with the Rietveld refinement of PXRD patterns.

ABBREVIATIONS

OAm, oleylamine; DDT, dodecanethiol; NN, nearest neighbor; NCs, nanocrystals; EXAFS, extended X-ray absorption fine structure; PXRD, powder X-ray diffraction; STEM, scanning transmission electron microscopy; EDS, energy dispersive X-ray spectroscopy; FTIR, Fourier-transform infrared spectroscopy; ¹H NMR, proton nuclear magnetic resonance spectroscopy

REFERENCES

- (1) Tolle, J.; Chizmeshya, A. V. G.; Fang, Y. Y.; Kouvetakis, J.; D'Costa, V. R.; Hu, C. W.; Menéndez, J.; Tsong, I. S. T. Low Temperature Chemical Vapor Deposition of Si-Based Compounds Via SiH₃SiH₂SiH₃: Metastable SiSn/GeSn/Si(100) Heteroepitaxial Structures. *Appl. Phys. Lett.* **2006**, *89*, 231924.
- (2) Moontragoon, P.; Ikonić, Z.; Harrison, P. Band Structure Calculations of Si–Ge–Sn Alloys: Achieving Direct Band Gap Materials. *Semicond. Sci. Technol.* **2007**, *22*, 742-748.
- (3) Lee, M.-H.; Liu, P.-L.; Hong, Y.-A.; Chou, Y.-T.; Hong, J.-Y.; Siao, Y.-J. Electronic Band Structures of $Ge_{1-x}Sn_x$ Semiconductors: A First-Principles Density Functional Theory Study. *J. Appl. Phys.* **2013**, *113*, 063517.
- (4) Cheng, R.; Wang, W.; Gong, X.; Sun, L.; Guo, P.; Hu, H.; Shen, Z.; Han, G.; Yeo, Y.-C. Relaxed and Strained Patterned Germanium-Tin Structures: A Raman Scattering Study. *ECS Journal of Solid State Science and Technology* **2013**, *2*, P138-P145.
- (5) Gupta, S.; Chen, R.; Huang, Y.-C.; Kim, Y.; Sanchez, E.; Harris, J. S.; Saraswat, K. C. Highly Selective Dry Etching of Germanium over Germanium–Tin ($Ge_{1-x}Sn_x$): A Novel Route for $Ge_{1-x}Sn_x$ Nanostructure Fabrication. *Nano Lett.* **2013**, *13*, 3783-3790.
- (6) Gupta, S.; Magyari-Köpe, B.; Nishi, Y.; Saraswat, K. C. Achieving Direct Band Gap in Germanium through Integration of Sn Alloying and External Strain. *J. Appl. Phys.* **2013**, *113*, 073707.
- (7) Barth, S.; Seifner, M. S.; Maldonado, S. Metastable Group IV Allotropes and Solid Solutions: Nanoparticles and Nanowires. *Chem. Mater.* **2020**, *32*, 2703-2741.
- (8) Spera, D. Z.; Arachchige, I. U., Colloidal Synthesis, Physical Properties, and Applications of Zero- and One-Dimensional GeSn

- Nanostructures. *Journal of Vacuum Science & Technology B* **2020**, *38*, 030802.
- (9) Doherty, J.; Biswas, S.; Galluccio, E.; Broderick, C. A.; Garcia-Gil, A.; Duffy, R.; O'Reilly, E. P.; Holmes, J. D. Progress on Germanium–Tin Nanoscale Alloys. *Chem. Mater.* **2020**.
- (10) Eckhardt, C.; Hummer, K.; Kresse, G. Indirect-to-Direct Gap Transition in Strained and Unstrained Sn_xGe_{1-x} Alloys. *Phys. Rev. B* **2014**, *89*, 165201.
- (11) Denton, A. R.; Ashcroft, N. W. Vegard's Law. *Physical Review A* **1991**, *43*, 3161-3164.
- (12) Yin, W.-J.; Gong, X.-G.; Wei, S.-H. Origin of the Unusually Large Band-Gap Bowing and the Breakdown of the Band-Edge Distribution Rule in the Sn_xGe_{1-x} Alloys. *Phys. Rev. B* **2008**, *78*, 161203.
- (13) Chen, R.; Lin, H.; Huo, Y.; Hitzman, C.; Kamins, T. I.; Harris, J. S. Increased Photoluminescence of Strain-Reduced, High-Sn Composition Ge_{1-x}Sn_x Alloys Grown by Molecular Beam Epitaxy. *Appl. Phys. Lett.* **2011**, *99*, 181125.
- (14) Wirths, S., et al. Lasing in Direct-Bandgap GeSn Alloy Grown on Si. *Nature Photonics* **2015**, *9*, 88.
- (15) Lu Low, K.; Yang, Y.; Han, G.; Fan, W.; Yeo, Y.-C. Electronic Band Structure and Effective Mass Parameters of Ge_{1-x}Sn_x Alloys. *J. Appl. Phys.* **2012**, *112*, 103715.
- (16) Hafiz, S. A.; Esteves, R. J. A.; Demchenko, D. O.; Arachchige, I. U.; Özgür, Ü. Energy Gap Tuning and Carrier Dynamics in Colloidal $Ge_{1-x}Sn_x$ Quantum Dots. *The Journal of Physical Chemistry Letters* **2016**, *7*, 3295-3301.
- (17) Esteves, R. J. A.; Ho, M. Q.; Arachchige, I. U. Nanocrystalline Group IV Alloy Semiconductors: Synthesis and Characterization of Ge_{1-x}Sn_x Quantum Dots for Tunable Bandgaps. *Chem. Mater.* **2015**, *27*, 1559-1568.
- (18) Esteves, R. J. A.; Hafiz, S.; Demchenko, D. O.; Ozgur, U.; Arachchige, I. U. Ultra-Small $Ge_{1-x}Sn_x$ Quantum Dots with Visible Photoluminescence. *Chem. Commun.* **2016**, *52*, 11665-11668.
- (19) Demchenko, D. O.; Tallapally, V.; Esteves, R. J. A.; Hafiz, S.; Nakagawara, T. A.; Arachchige, I. U.; Özgür, Ü. Optical Transitions and Excitonic Properties of $Ge_{1-x}Sn_x$ Alloy Quantum Dots. *J. Phys. Chem. C* **2017**, *121*, 18299-18306.
- (20) Seifner, M. S.; Biegger, F.; Lugstein, A.; Bernardi, J.; Barth, S. Microwave-Assisted $Ge_{1-x}Sn_x$ Nanowire Synthesis: Precursor Species and Growth Regimes. *Chem. Mater.* **2015**, *27*, 6125-6130.
- (21) Tabatabaei, K.; Lu, H.; Nolan, B. M.; Cen, X.; McCold, C. E.; Zhang, X.; Brutchey, R. L.; van Benthem, K.; Hihath, J.; Kauzlarich, S. M. Bismuth Doping of Germanium Nanocrystals through Colloidal Chemistry. *Chem. Mater.* **2017**, *29*, 7353-7363.
- (22) Sully, H. R., et al. Characterizing Bismuth Doping of Colloidal Germanium Quantum Dots for Energy Conversion Applications. *ACS Applied Nano Materials* **2020**.
- (23) Olesinski, R. W.; Abbaschian, G. J. The Ge-Sn (Germanium-Tin) System. *Bulletin of Alloy Phase Diagrams* **1984**, *5*, 265-271.
- (24) Tallapally, V.; Nakagawara, T. A.; Demchenko, D. O.; Özgür, Ü.; Arachchige, I. U. $Ge_{1-x}Sn_x$ Alloy Quantum Dots with Composition-Tunable Energy Gaps and Near-Infrared Photoluminescence. *Nanoscale* **2018**, *10*, 20296-20305.
- (25) Yang, Q.; Zhao, X.; Wu, X.; Li, M.; Di, Q.; Fan, X.; Zhu, J.; Song, X.; Li, Q.; Quan, Z. Facile Synthesis of Uniform $Sn_{1-x}Ge_x$ Alloy Nanocrystals with Tunable Bandgap. *Chem. Mater.* **2019**, *31*, 2248-2252.
- (26) Zhao, X.; Yang, Q.; Quan, Z. Tin-Based Nanomaterials: Colloidal Synthesis and Battery Applications. *Chem. Commun.* **2019**, *55*, 8683-8694.
- (27) Barth, S.; Seifner, M. S.; Bernardi, J. Microwave-Assisted Solution–Liquid–Solid Growth of $Ge_{1-x}Sn_x$ Nanowires with High Tin Content. *Chem. Commun.* **2015**, *51*, 12282-12285.
- (28) Ruddy, D. A.; Erslev, P. T.; Habas, S. E.; Seabold, J. A.; Neale, N. R. Surface Chemistry Exchange of Alloyed Germanium Nanocrystals: A Pathway toward Conductive Group IV Nanocrystal Films. *J. Phys. Chem. Lett.* **2013**, *4*, 416-421.
- (29) Ramasamy, K.; Kotula, P. G.; Fidler, A. F.; Brumbach, M. T.; Pietryga, J. M.; Ivanov, S. A., Sn_xGe_{1-x} Alloy Nanocrystals: A First

- Step toward Solution-Processed Group IV Photovoltaics. *Chem. Mater.* **2015**, *27* (13), 4640-4649.
- (30) Ramasamy, K.; Kotula, P. G.; Fidler, A. F.; Brumbach, M. T.; Pietryga, J. M.; Ivanov, S. A. Sn_xGe_{1-x} Alloy Nanocrystals: A First Step toward Solution-Processed Group IV Photovoltaics. *Chem. Mater.* **2015**, *27*, 4640-4649.
- (31) Boote, B. W.; Men, L.; Andaraarachchi, H. P.; Bhattacharjee, U.; Petrich, J. W.; Vela, J.; Smith, E. A. Germanium–Tin/Cadmium Sulfide Core/Shell Nanocrystals with Enhanced Near-Infrared Photoluminescence. *Chem. Mater.* **2017**, *29*, 6012-6021.
- (32) Muthuswamy, E.; Zhao, J.; Tabatabaei, K.; Amador, M. M.; Holmes, M. A.; Osterloh, F. E.; Kauzlarich, S. M. Thiol-Capped Germanium Nanocrystals: Preparation and Evidence for Quantum Size Effects. *Chem. Mater.* **2014**, *26*, 2138-2146.
- (33) Holmes, A. L.; Hütges, J.; Reckmann, A.; Muthuswamy, E.; Meerholz, K.; Kauzlarich, S. M. Probing Electronics as a Function of Size and Surface of Colloidal Germanium Nanocrystals. *J. Phys. Chem. C* **2015**, *119*, 5671-5678.
- (34) Newton, K. A.; Ju, Z.; Tabatabaei, K.; Kauzlarich, S. M. Diorganyl Dichalcogenides as Surface Capping Ligands for Germanium Nanocrystals. *Organometallics* **2020**, *39*, 995-1005.
- (35) Smock, S. R.; Tabatabaei, K.; Williams, T. J.; Kauzlarich, S. M.; Brutchey, R. L. Surface Coordination Chemistry of Germanium Nanocrystals Synthesized by Microwave-Assisted Reduction in Oleylamine. *Nanoscale* **2020**, *12*, 2764-2772.
- (36) Restrepo, D. T.; Lynch, K. E.; Giesler, K.; Kuebler, S. M.; Blair, R. G. Low-Temperature (210°C) Deposition of Crystalline Germanium Via In Situ Disproportionation of Gel_2 . *Mater. Res. Bull.* **2012**, 47, 3484-3488.
- (37) Jade 5.0, 5.0.37 ed.; Materials Data Inc.: Livermore, CA, 2004
- (38) Petricek, V.; Dusek, M.; Palatinus, L. *Jana2006*, 25/10/2015 ed.; Institute of Physics, Academy of Sciences of the Czech Republic: Prague, Czech Republic, 2006.
- (39) Yoder-Short, D. On a Small Error in SRM640, SRM640a and SRM640b Lattice Parameters. *J. Appl. Crystallogr.* **1993**, *26*, 272-276.
- (40) *Inorganic Crystal Structure Database (ICSD)*; FIZ Karlsruhe-Leibniz Institute for Information Infrastructure: Eggenstein-Leopoldshafen, Germany, 2019.
- (41) Rasband, W. *ImageJ*, 1.52a ed.; National Institutes of Health: Bethesda, MD, USA.
 - (42) AZtec 3.3; Oxford Instruments NanoAnalysis: Concord, MA.
- (43) R-Space X-Ray Absorption Package; Lawrence Berkeley National Laboratory: Berkeley, CA, 2010.
- (44) Ankudinov, A. L.; Rehr, J. J. Relativistic Calculations of Spin-Dependent X-Ray-Absorption Spectra. *Phys. Rev. B* **1997**, *56*, R1712-R1716.
- (45) Mathematica, 11.0.1.0 ed.; Wolfram Research, Inc.: Champaign, Illinois, 2016.
- (46) Tabatabaei, K.; Holmes, A. L.; Newton, K. A.; Muthuswamy, E.; Sfadia, R.; Carter, S. A.; Kauzlarich, S. M. Halogen-Induced Crystallinity and Size Tuning of Microwave Synthesized Germanium Nanocrystals. *Chem. Mater.* **2019**, *31*, 7510-7521.
- (47) *Mestrenova*, 10.0.2-15465 ed.; Mestrelab Research S. L.: Santiago de Compostela, Spain, 2015.
- (48) Tauc, J. Optical Properties and Electronic Structure of Amorphous Ge and Si. *Mater. Res. Bull.* **1968**, *3*, 37-46.
- (49) Cooper, A. Precise Lattice Constants of Germanium, Aluminum, Gallium Arsenide, Uranium, Sulphur, Quartz and Sapphire. *Acta Crystallographica* **1962**, *15*, 578-582.
- (50) Thewlis, J.; Davey, A. R. Thermal Expansion of Grey Tin. *Nature* **1954**, *174*, 1011-1011.
- (51) Aella, P.; Cook, C.; Tolle, J.; Zollner, S.; Chizmeshya, A. V. G.; Kouvetakis, J. Optical and Structural Properties of $Si_xSn_yGe_{1-x-y}$ Alloys. *Appl. Phys. Lett.* **2004**, *84*, 888-890.
- (52) Gencarelli, F.; Grandjean, D.; Shimura, Y.; Vincent, B.; Banerjee, D.; Vantomme, A.; Vandervorst, W.; Loo, R.; Heyns, M.; Temst, K. Extended X-Ray Absorption Fine Structure Investigation

- of Sn Local Environment in Strained and Relaxed Epitaxial $Ge_{1-x}Sn_x$ Films. *J. Appl. Phys.* **2015**, *117*, 095702.
- (53) Downward, L.; Booth, C. H.; Lukens, W. W.; Bridges, F. A Variation of the F-Test for Determining Statistical Relevance of Particular Parameters in EXAFS Fits. *AIP Conference Proceedings* **2007**, *882*, 129-131.
- (54) Zhang, Y.; Karatutlu, A.; Ersoy, O.; Little, W.; Cibin, G.; Dent, A.; Sapelkin, A. Structure and Effects of Annealing in Colloidal Matrix-Free Ge Quantum Dots. *Journal of Synchrotron Radiation* **2015**, *22*, 105-112.
- (55) Zhang, Y.; Ersoy, O.; Karatutlu, A.; Little, W.; Sapelkin, A. Local Structure of Ge Quantum Dots Determined by Combined Numerical Analysis of EXAFS and XANES Data. *Journal of Synchrotron Radiation* **2016**, *23*, 253-259.
- (56) Tabatabaei, K.; Sully, H. R.; Ju, Z.; Hellier, K.; Lu, H.; Perez, C. J.; Newton, K. A.; Brutchey, R. L.; Bridges, F.; Carter, S. A.; Kauzlarich, S. M. Structural Insights on Microwave-Synthesized Antimony-Doped Germanium Nanocrystals. *ACS Nano* **2021**, *15* (1), 1685-1700.
- (57) Stern, E. A.; Bouldin, C. E.; von Roedern, B.; Azoulay, J. Incipient Amorphous-to-Crystalline Transition in Ge. *Phys. Rev. B* **1983**, *27*, 6557-6560.
- (58) Lignie, A.; Ménaert, B.; Armand, P.; Peña, A.; Debray, J.; Papet, P. Top Seeded Solution Growth and Structural Characterizations of α -Quartz-Like Structure GeO₂ Single Crystal. *Crystal Growth & Design* **2013**, *13*, 4220-4225.
- (59) Bottani, C. E.; Bassi, A. L.; Stella, A.; Cheyssac, P.; Kofman, R. Investigation of Confined Acoustic Phonons of Tin Nanoparticles During Melting. *Europhysics Letters (EPL)* **2001**, *56*, 386-392.
- (60) Diéguez, A.; Romano-Rodríguez, A.; Vilà, A.; Morante, J. R. The Complete Raman Spectrum of Nanometric SnO₂ Particles. *J. Appl. Phys.* **2001**, *90*, 1550-1557.
- (61) Ma, X.; Wu, F.; Kauzlarich, S. M. Alkyl-Terminated Crystalline Ge Nanoparticles Prepared from NaGe: Synthesis, Functionalization and Optical Properties. *J. Solid State Chem.* **2008**, *181*, 1628-1633.
- (62) Pescara, B.; Mazzio, K. A.; Lips, K.; Raoux, S. Crystallinity and Size Control of Colloidal Germanium Nanoparticles from Organogermanium Halide Reagents. *Inorg. Chem.* **2019**, *58*, 4802-4811.
- (63) D'Costa, V. R.; Tolle, J.; Roucka, R.; Poweleit, C. D.; Kouvetakis, J.; Menéndez, J. Raman Scattering in Ge_{1-y}Sn_y Alloys. *Solid State Commun.* **2007**, *144*, 240-244.
- (64) Menéndez, J.; Höchst, H. Study of the Phase Transition in Heteroepitaxially Grown Films of α -Sn by Raman Spectroscopy. *Thin Solid Films* **1984**, *111*, 375-379.
- (65) Corsini, N. R. C., et al. Pressure-Induced Amorphization and a New High Density Amorphous Metallic Phase in Matrix-Free Ge Nanoparticles. *Nano Lett.* **2015**, *15*, 7334-7340.
- (66) Sasaki, Y.; Horie, C. Resonant Raman Study of Phonon States in Gas-Evaporated Ge Small Particles. *Phys. Rev. B* **1993**, *47*, 3811-3818.
- (67) Pizzagalli, L.; Galli, G. Surface Reconstruction Effects on Atomic Properties of Semiconducting Nanoparticles. *Materials Science and Engineering: B* **2002**, *96*, 86-89.
- (68) Gassenq, A., et al. Raman Spectral Shift Versus Strain and Composition in GeSn Layers with 6%–15% Sn Content. *Appl. Phys. Lett.* **2017**, *110*, 112101.
- (69) Perova, T. S.; Kasper, E.; Oehme, M.; Cherevkov, S.; Schulze, J. Features of Polarized Raman Spectra for Homogeneous and Non-Homogeneous Compressively Strained Ge_{1-y}Sn_y Alloys. *Journal of Raman Spectroscopy* **2017**, *48*, 993-1001.
- (70) Kanakaraju, S.; Sood, A. K.; Mohan, S. In Situ Raman Monitoring of Ultrathin Ge Films. *J. Appl. Phys.* **1998**, *84*, 5756-5760.
- (71) Takeuchi, K.; Kosemura, D.; Yokogawa, R.; Usuda, K.; Ogura, A. Origin of Additional Broad Peaks in Raman Spectra from Thin Germanium-Rich Silicon–Germanium Films. *Applied Physics Express* **2016**, *9*, 071301.

- (72) Fujii, M.; Hayashi, S.; Yamamoto, K. Raman Scattering from Quantum Dots of Ge Embedded in SiO₂ Thin Films. *Appl. Phys. Lett.* **1990**, *57*, 2692-2694.
- (73) Campbell, I. H.; Fauchet, P. M. The Effects of Microcrystal Size and Shape on the One Phonon Raman Spectra of Crystalline Semiconductors. *Solid State Commun.* **1986**, *58*, 739-741.
- (74) Rojas-López, M.; Navarro-Contreras, H.; Desjardins, P.; Gurdal, O.; Taylor, N.; Carlsson, J. R. A.; Greene, J. E. Raman Scattering from Fully Strained $Ge_{1-x}Sn_x$ ($x \le 0.22$) Alloys Grown on $Ge(001)2 \times 1$ by Low-Temperature Molecular Beam Epitaxy. *J. Appl. Phys.* **1998**, *84*, 2219-2223.
- (75) Li, S. F.; Bauer, M. R.; Menéndez, J.; Kouvetakis, J. Scaling Law for the Compositional Dependence of Raman Frequencies in SnGe and GeSi Alloys. *Appl. Phys. Lett.* **2004**, *84*, 867-869.
- (76) Gorokhov, E. B.; Volodin, V. A.; Marin, D. V.; Orekhov, D. A.; Cherkov, A. G.; Gutakovskii, A. K.; Shvets, V. A.; Borisov, A. G.; Efremov, M. D. Effect of Quantum Confinement on Optical Properties of Ge Nanocrystals in GeO_2 Films. *Semiconductors* **2005**, *39*, 1168-1175.
- (77) Volodin, V. A.; Marin, D. V.; Sachkov, V. A.; Gorokhov, E. B.; Rinnert, H.; Vergnat, M. Applying an Improved Phonon Confinement Model to the Analysis of Raman Spectra of Germanium Nanocrystals. *Journal of Experimental and Theoretical Physics* **2014**, *118*, 65-71.
- (78) Ou, H.; Ou, Y.; Liu, C.; Berg, R. W.; Rottwitt, K. Formation and Characterization of Varied Size Germanium Nanocrystals by Electron Microscopy, Raman Spectroscopy, and Photoluminescence. *Optical Materials Express* **2011**, *1*, 643-651.
- (79) Serincan, U.; Kartopu, G.; Guennes, A.; Finstad, T. G.; Turan, R.; Ekinci, Y.; Bayliss, S. C. Characterization of Ge Nanocrystals Embedded in SiO₂ by Raman Spectroscopy. *Semicond. Sci. Technol.* **2003**, *19*, 247-251.
- (80) He, M.; Protesescu, L.; Caputo, R.; Krumeich, F.; Kovalenko, M. V. A General Synthesis Strategy for Monodisperse Metallic and Metalloid Nanoparticles (In, Ga, Bi, Sb, Zn, Cu, Sn, and Their Alloys) Via In Situ Formed Metal Long-Chain Amides. *Chem. Mater.* **2015**, *27*, 635-647.
- (81) Bernard, A.; Zhang, K.; Larson, D.; Tabatabaei, K.; Kauzlarich, S. M. Solvent Effects on Growth, Crystallinity, and Surface Bonding of Ge Nanoparticles. *Inorg. Chem.* **2018**.
- (82) Valdez, C. N.; Schimpf, A. M.; Gamelin, D. R.; Mayer, J. M. Low Capping Group Surface Density on Zinc Oxide Nanocrystals. *ACS Nano* **2014**, *8*, 9463-9470.
- (83) De Roo, J., et al. Probing Solvent–Ligand Interactions in Colloidal Nanocrystals by the NMR Line Broadening. *Chem. Mater.* **2018**, *30*, 5485-5492.
- (84) De Roo, J.; Coucke, S.; Rijckaert, H.; De Keukeleere, K.; Sinnaeve, D.; Hens, Z.; Martins, J. C.; Van Driessche, I. Amino Acid-Based Stabilization of Oxide Nanocrystals in Polar Media: From Insight in Ligand Exchange to Solution ¹H NMR Probing of Short-Chained Adsorbates. *Langmuir* **2016**, *32*, 1962-1970.
- (85) Mo, L.; Liu, D.; Li, W.; Li, L.; Wang, L.; Zhou, X. Effects of Dodecylamine and Dodecanethiol on the Conductive Properties of Nano-Ag Films. *Appl. Surf. Sci.* **2011**, *257*, 5746-5753.
- (86) Mourdikoudis, S.; Liz-Marzán, L. M. Oleylamine in Nanoparticle Synthesis. *Chem. Mater.* **2013**, *25*, 1465-1476.

- (87) Shukla, N.; Liu, C.; Jones, P. M.; Weller, D. FTIR Study of Surfactant Bonding to FePt Nanoparticles. *J. Magn. Magn. Mater.* **2003**, *266*. 178-184.
- (88) Ohkaku, N.; Nakamoto, K. Metal Isotope Effect on Metal-Liquid Vibrations. X. Far-Infrared Spectra of Trans Adducts of Tin(IV) Tetrahalide with Unidentate Ligands. *Inorg. Chem.* **1973**, *12*, 2440-2446.
- (89) Muthuswamy, E.; Iskandar, A. S.; Amador, M. M.; Kauzlarich, S. M. Facile Synthesis of Germanium Nanoparticles with Size Control: Microwave Versus Conventional Heating. *Chem. Mater.* **2013**, *25*, 1416-1422.
- (90) Chiu, Y.-W.; Huang, M. H. Formation of Hexabranched GeO₂ Nanoparticles Via a Reverse Micelle System. *J. Phys. Chem. C* **2009**, *113*, 6056-6060.
- (91) Wu, H. P.; Liu, J. F.; Ge, M. Y.; Niu, L.; Zeng, Y. W.; Wang, Y. W.; Lv, G. L.; Wang, L. N.; Zhang, G. Q.; Jiang, J. Z. Preparation of Monodisperse GeO_2 Nanocubes in a Reverse Micelle System. *Chem. Mater.* **2006**, *18*, 1817-1820.
- (92) Wu, W., et al. Simple Synthesis and Luminescence Characteristics of PVP-Capped GeO₂ Nanoparticles. *J. Nanomater.* **2011**, *2011*, 5.
- (93) Zhang, B.; Tian, Y.; Zhang, J. X.; Cai, W. The FTIR Studies of SnO₂:Sb(ATO) Films Deposited by Spray Pyrolysis. *Mater. Lett.* **2011**, *65*, 1204-1206.
- (94) Kuantama, E.; Han, D.-W.; Sung, Y.-M.; Song, J.-E.; Han, C.-H. Structure and Thermal Properties of Transparent Conductive Nanoporous F:SnO₂ Films. *Thin Solid Films* **2009**, *517*, 4211-4214.
- (95) Ocaña, M.; Serna, C. J. Variations of the Infrared Powder Spectra of TiO₂ and SnO₂ (Rutile) with Polarization. *Spectrochimica Acta Part A: Molecular Spectroscopy* **1991**, *47*, 765-774.
- (96) Paramarta, V.; Taufik, A.; Saleh, R. Better Adsorption Capacity of SnO₂ Nanoparticles with Different Graphene Addition. *Journal of Physics: Conference Series* **2016**, *776*, 012039.
- (97) Ibarguen, C. A.; Mosquera, A.; Parra, R.; Castro, M. S.; Rodríguez-Páez, J. E. Synthesis of SnO_2 Nanoparticles through the Controlled Precipitation Route. *Mater. Chem. Phys.* **2007**, *101*, 433-440
- (98) Xu, D.; Liu, Z.; Liang, J.; Qian, Y. Solvothermal Synthesis of CdS Nanowires in a Mixed Solvent of Ethylenediamine and Dodecanethiol. *J. Phys. Chem. B* **2005**, *109*, 14344-14349.
- (99) Yang, L.; Guihen, E.; Glennon, J. D. Alkylthiol Gold Nanoparticles in Sol-Gel-Based Open Tubular Capillary Electrochromatography. *J. Sep. Sci.* **2005**, *28*, 757-766.
- (100) Yang, J.; Ling, T.; Wu, W.-T.; Liu, H.; Gao, M.-R.; Ling, C.; Li, L.; Du, X.-W. A Top–Down Strategy Towards Monodisperse Colloidal Lead Sulphide Quantum Dots. *Nature Communications* **2013**, *4*, 1695.
- (101) Xu, J.; Almeida, R. M. Preparation and Characterization of Germanium Sulfide Based Sol-Gel Planar Waveguides. *J. Sol-Gel Sci. Technol.* **2000**, *19*, 243-248.
- (102) Kovala-Demertzi, D.; Tauridou, P.; Russo, U.; Gielen, M. Adducts of Organotin(IV), Tin(IV) and Tin(II) Halides with 1-Methyl-Imidazoline-2(3H)-Thione (Hmimt) and Imidazoline-2(1,3H)-Thione (Himt). Synthesis, Spectroscopic (IR, Mössbauer and ¹H, ¹³C, ¹¹⁹Sn NMR) Studies and In Vitro Antitumour Activity. *Inorg. Chim. Acta* **1995**, *239*, 177-183.

TOC Graphic

